

The EBEX Balloon Borne Experiment - Detectors and Readout

The EBEX Collaboration: Maximilian Abitbol¹, Asad M. Aboobaker^{2,3*}, Peter Ade⁴, Derek Araujo¹, François Aubin^{5,2*,†}, Carlo Baccigalupi^{6,7}, Chaoyun Bao², Daniel Chapman¹, Joy Didier^{1,8*}, Matt Dobbs^{5,9}, Stephen M. Feeney^{10,11*}, Christopher Geach², Will Grainger⁴, Shaul Hanany², Kyle Helson^{12,13*}, Seth Hillbrand¹, Gene Hilton¹⁴, Johannes Hubmayr¹⁴, Kent Irwin^{14,15*}, Andrew Jaffe¹⁰, Bradley Johnson¹, Terry Jones², Jeff Klein², Andrei Korotkov¹², Adrian Lee¹⁶, Lorne Levinson¹⁷, Michele Limon¹, Kevin MacDermid⁵, Amber D. Miller^{1,8*}, Michael Milligan², Kate Raach², Britt Reichborn-Kjennerud¹, Carl Reintsema¹⁴, Ilan Sagiv¹⁷, Graeme Smecher⁵, Gregory S. Tucker¹², Benjamin Westbrook¹⁶, Karl Young², Kyle Zilic²

ABSTRACT

EBEX was a long-duration balloon-borne experiment to measure the polarization of the cosmic microwave background. The experiment had three frequency bands operating at 150, 250, and 410 GHz and was the first to use a kilo-pixel array of transition edge sensor bolometers aboard a balloon platform. The array was read out with a frequency domain multiplexing (FDM) system. We describe the design and characterization of the array and the readout system. We give the distributions of measured

¹Physics Department, Columbia University, New York, NY 10027

²School of Physics and Astronomy, University of Minnesota-Twin Cities, Minneapolis, MN 55455

³Jet Propulsion Laboratory, California Institute of Technology, Pasadena, CA 91109

⁴Rutherford Appleton Lab, Harwell Oxford, OX11 0QX, United Kingdom

⁵Department of Physics, McGill University, Montreal, H3A 2T8, Canada

⁶Astrophysics Sector, SISSA, Trieste, 34014, Italy

⁷INFN, Sezione di Trieste, Via Valerio 2, I-34127 Trieste, Italy

⁸Department of Physics and Astronomy, University of Southern California, Los Angeles, CA 90089

⁹Canadian Institute for Advanced Research, Toronto, M5G 1Z8, Canada

¹⁰Department of Physics, Imperial College, London, SW7 2AZ, United Kingdom

¹¹Center for Computational Astrophysics, Flatiron Institute, New York, NY 10010

¹²Department of Physics, Brown University, Providence, RI 02912

¹³NASA Goddard Space Flight Center, Greenbelt, MD 20771

¹⁴National Institute of Standards and Technology, Boulder, CO 80305

¹⁵Department of Physics, Stanford University, Stanford, CA 94305

¹⁶Department of Physics, University of California, Berkeley, CA 94720

¹⁷Faculty of Physics, Weizmann Institute of Science, Rehovot, 76100, Israel

*Current affiliation

†Corresponding Author: François Aubin (faubin@umn.edu)

thermal conductances, normal resistances, and transition temperatures. From the lowest to highest frequency, the median measured average thermal conductances were 39, 53, and 63 pW/K, the medians of transition temperatures were 0.45, 0.48, and 0.47 K, and the medians of normal resistances were 1.9, 1.5, and 1.4 Ω . With the exception of the thermal conductance at 150 GHz, all measured values are within 30% of their design. We measured median low loop-gain time constants $\tau_0 = 88, 46$, and 57 ms and compare them to predictions. Two measurements of bolometer absorption efficiency gave results consistent within 10% and showing high (~ 0.9) efficiency at 150 GHz and medium (~ 0.35 , and ~ 0.25) at the two higher bands, respectively. We measure a median total optical load of 3.6, 5.3 and 5.0 pW absorbed at the three bands, respectively. EBEX pioneered the use of the digital version of the FDM system. The system multiplexed the bias and readout of 16 bolometers onto two wires. We present accounting of the measured noise equivalent power and compare it to predictions. The median noise equivalent temperatures referred to a black body with a temperature of 2.725 K are 400, 920, and 14500 $\mu\text{K}\sqrt{s}$ for the three bands, respectively. We compare these values to our pre-flight predictions and to a previous balloon payload, discuss the sources of excess noise, and the path for a future payload to make full use of the balloon environment.

Subject headings: balloons - cosmic background radiation - cosmology: observations - instrumentation: polarimeters - frequency domain readout system - transition-edge sensor bolometers

1. Introduction

Measurements of the cosmic microwave background (CMB) have provided a wealth of information about the physical mechanisms responsible for the evolution of the Universe. In recent years, experimental efforts have focused on measuring the CMB’s polarization patterns: *E*-modes and *B*-modes (Zaldarriaga & Seljak 1997). The level and specific shape of the angular power spectrum of CMB *E*-mode polarization can be predicted given the measured intensity anisotropy. Lensing of *E*-modes by the large scale structure of the Universe produces cosmological *B*-modes at small angular scales, while an inflationary phase at sufficiently high energy scales near the big bang is predicted to leave another perhaps detectable *B*-mode signature at large and intermediate angular scales (Baumann et al. 2009).

The *E*-mode polarization of the CMB was first detected by the DASI experiment (Kovac et al. 2002), and other experiments soon followed suit (Scott & Smoot 2010). The combination of all measurements is in excellent agreement with predictions. *B*-mode polarization from gravitational lensing of *E*-modes and from Galactic dust emission has also recently been detected (Hanson et al. 2013; Ade et al. 2014; Naess et al. 2014; BICEP2 Collaboration et al. 2014; BICEP2/Keck and Planck Collaborations et al. 2015). Intense efforts are ongoing by ground- and balloon-based instruments to improve the measurements, separate the Galactic from the cosmological signals, and identify the inflationary *B*-mode signature.

The E and B Experiment (EBEX) was a balloon-borne CMB polarimeter designed to detect or constrain the levels of the inflationary gravitational wave and lensing B -mode power spectra. EBEX was also designed to be a technology pathfinder for future CMB space missions. To achieve instrument sensitivity, we implemented a kilo-pixel array of transition edge sensor (TES) bolometers and planned for a long duration balloon flight. We included three spectral bands centered on 150, 250, and 410 GHz to give sensitivity to both the CMB and the galactic dust foreground. The combination of the 400 deg² intended survey size and an optical system with 0.1° resolution gave sensitivity to the range $30 < \ell < 1500$ of the angular power spectrum. Polarimetry was achieved with a continuously rotating achromatic half-wave plate (HWP) and a wire grid analyzer.

Design and construction of the experiment began in 2005. A ten-hour engineering flight was launched from Ft. Sumner, NM on June 11, 2009, and the long-duration science flight was launched from McMurdo Station, Antarctica on December 29, 2012. Data collection ceased when cryogenics expired after 11 days, as planned. Because the majority of the flight occurred during January 2013, we refer to this flight as EBEX2013.

This paper is one of a series of papers describing the experiment and its in-flight performance. This paper, called EBEX Paper 2 (EP2), discusses the detectors and readout; EBEX Paper 1 (EP1) (The EBEX Collaboration 2016a) describes the optical system, the receiver, and the polarimetric approach; EBEX Paper 3 (EP3) (The EBEX Collaboration 2016b), gives information about the gondola, the attitude control system, and other support systems. A fourth paper, EBEX Paper 4 (EP4) (Didier et al. 2017) discusses effects associated with detector non-linearity and their influence on polarimetric measurements. Several other publications give additional details about EBEX. Some are from earlier stages of the program (Oxley et al. 2004; Hubmayr et al. 2008; Grainger et al. 2008; Aubin et al. 2010; Milligan et al. 2010; Reichborn-Kjennerud et al. 2010; Klein et al. 2011; Sagiv et al. 2012; Westbrook et al. 2012), and others discuss some subsystems in more detail (Polsgrove 2009; Reichborn-Kjennerud 2010; Sagiv 2011; Aubin 2012; MacDermid 2014; MacDermid et al. 2014; Westbrook 2014; Zilic 2014; Chapman et al. 2014; Chapman 2015; Chapman et al. 2015; Didier et al. 2015; Didier 2016; Aubin et al. 2016).

Several new technologies have been implemented and tested for the first time in the EBEX instrument. It was the first astrophysical instrument to implement and operate a superconducting magnetic bearing (SMB), which was used to levitate the HWP. This system was discussed in EP1. EBEX was also the first balloon-borne experiment to implement a kilo-pixel array of TES bolometric detectors and it was the first to implement a digital frequency domain multiplexing system to read out the TES arrays. The implementation of these new technologies aboard a balloon flight presented several new challenges. These included the development of detectors that were optimized for the smaller optical loading at the stratosphere and that were tuned to operate at higher frequency bands compared to those typically used on ground-based instruments, and the development of a readout system with as low power dissipation per channel as realistically implementable while still giving low noise and low $1/f$ knee.

This paper describes our implementation of the readout system, and the design and characterization of the bolometers. In Section 2 we give a brief overview of the instrument, its optical system, and the design of the focal plane. Section 3 gives the characteristics of the time domain

data and describes the processing that was necessary to extract time-domain noise levels. The implementation of the readout system and an assessment of its noise and gain stability are the subject of Section 4. In Section 5 we discuss the design of the detectors and give results from laboratory characterization measurements. We also describe the measured in-flight radiative load and use this measurement as one of three approaches to extract the bolometer absorption efficiencies. We end this Section with a discussion of the measured noise equivalent power. In Section 6 we report our measurements of the noise equivalent temperature and the final map depth at each of the three frequency bands. We discuss and summarize our findings in Section 7.

2. The EBEX Instrument and Focal Planes

The EBEX optical system consisted of a 105 cm aperture off-axis Gregorian telescope coupled to a cryogenic receiver containing refractive optics, a rotating achromatic HWP at a cold aperture stop, and a polarizing grid that directed independent polarizations to each of two focal planes cooled to a bath temperature of ~ 0.25 K; see Figure 1. The focal planes were referred to as the H (horizontal) and V (vertical) focal planes. The optical and cryogenic systems are described in detail in EP1.

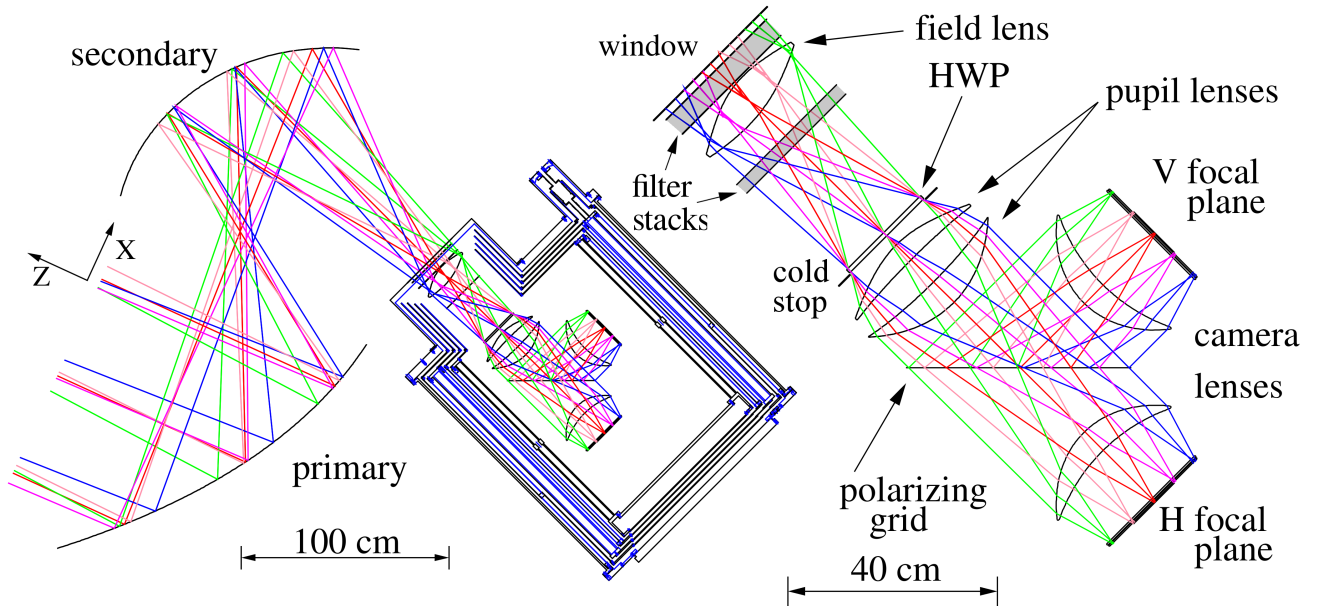


Fig. 1.— Left: ray tracing of the EBEX optical design consisting of two ambient temperature reflectors in a Gregorian configuration and a cryogenic receiver. Right: inside the receiver, cryogenically cooled polyethylene lenses formed a cold stop and provided diffraction limited performance over a flat, telecentric, 6.6° field of view. Two identical focal planes (H and V) terminated the optical path.

Figure 2 shows the elements of a focal plane. It consisted of a layer of electromagnetic filters, a monolithic array of feedhorns attached to a monolithic array of waveguides, 7 detector wafers

coupled to wafer holders and inductor and capacitor (LC) boards, and a back cover. The back cover, together with the array of horns, completed a Faraday cage around the focal plane. The electromagnetic filters and waveguides defined frequency bands centered on 150, 250, and 410 GHz. Each focal plane was arranged such that 4 wafers operated at 150 GHz, 2 at 250 GHz, and 1 at 410 GHz; see Figure 2. The LC boards were part of the multiplexed frequency domain bias and readout of the detectors, see Section 4. Each detector wafer had 140 lithographically fabricated bolometers of which up to 127 could be biased and read out with 8 pairs of wires, see Section 5.2.

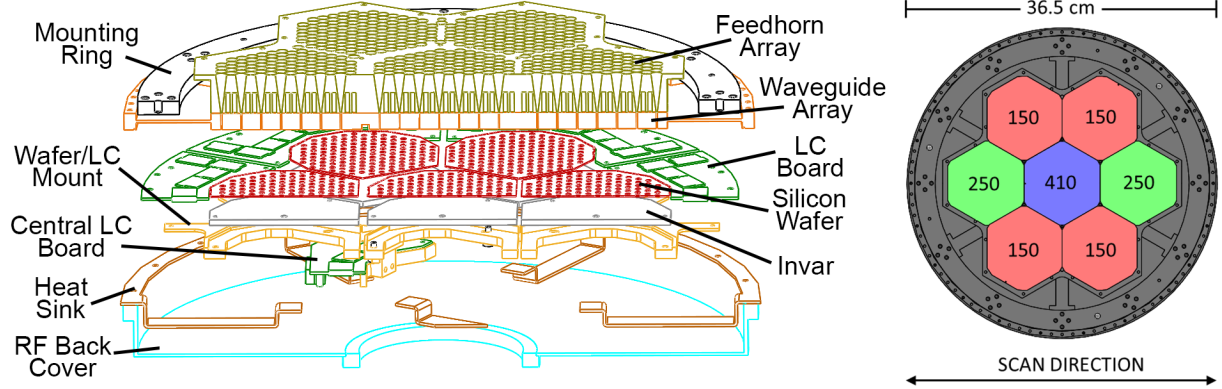


Fig. 2.— Left: a solid model cross section through one of the EBEX focal planes. Right: sketch of a photon view. The instrument had two identical focal planes. The colors of the hexagons (and numbers) encode frequency bands (in GHz).

Each TES bolometer had a pair of electrical lines lithographed with niobium connected to bond pads at the edge of its wafer. Wire bonds connected the wafer to an LC board, which contained inductors and capacitors that were part of the frequency domain multiplexing readout; see Section 4. We placed each silicon wafer onto a wafer-shaped piece of Invar thinly coated with warmed Apiezon N grease. For the edge wafers, the Invar was screwed into an aluminum mount holding the LC board in the same plane as the wafers. For the central wafer, we mounted the LC board below this plane with standoffs. To align the wafers with the feedhorns, we doweled the wafer’s aluminum mount to a jig that simulated the waveguide array but had fewer, larger holes. We warmed the Invar and nudged the wafers until the bolometers were aligned with the alignment holes. The same alignment dowels that were used with the jig were later used with the waveguide and feedhorn array. We soldered to the LC boards a commercially made microstrip with copper traces that was terminated with a micro-D connector. An additional set of self-made microstrips with niobium wires, which are described in Section 4.1, transmitted the signals to the superconducting quantum interference device (SQUID) boards. Commercial wire harnesses with manganin twisted pairs embedded in a Nomex weave connected the SQUID boards to the room temperature readout electronics.

3. The Time Domain Data

During polarimetric observations we rotated the HWP at $f_{HWP} = 1.235$ Hz. The combination of this rotation and the fixed polarizing grid modulated the polarized radiation incident on the HWP at frequency $4f_{HWP}$ in the bolometer time ordered data (TOD). Sources of incident polarized

radiation included polarized sky sources, such as the galaxy and the CMB, polarized emission by the instrument, primarily arising from the two reflectors, and sources of instrumental polarization. The primary source of instrumental polarization was the field lens as described in EP1, but there were small contributions from the reflectors and the vacuum window as well. The instrument polarized emissions and instrumental polarization were much more intense than both polarized sky emissions and instrument noise. Figure 3 shows the typical characteristics of the calibrated TOD during a period in which the HWP was rotating. A large amplitude signal that is synchronous with the rotation of the HWP, and which we call half-wave plate synchronous signal (HWPSS), is apparent at harmonics of the HWP rotation frequency and is due to the mostly time stable instrumental polarization and instrumental polarized emission. The spectral density of the TOD, also given in Figure 3, shows that the amplitude of the HWPSS is orders of magnitude larger than the white noise level. The maximum galactic signal at 150 GHz is expected to be 0.3 fW, also much smaller than the HWPSS. Didier (2016), Araujo (2017), and Didier et al. (2017) give more information about the HWPSS.

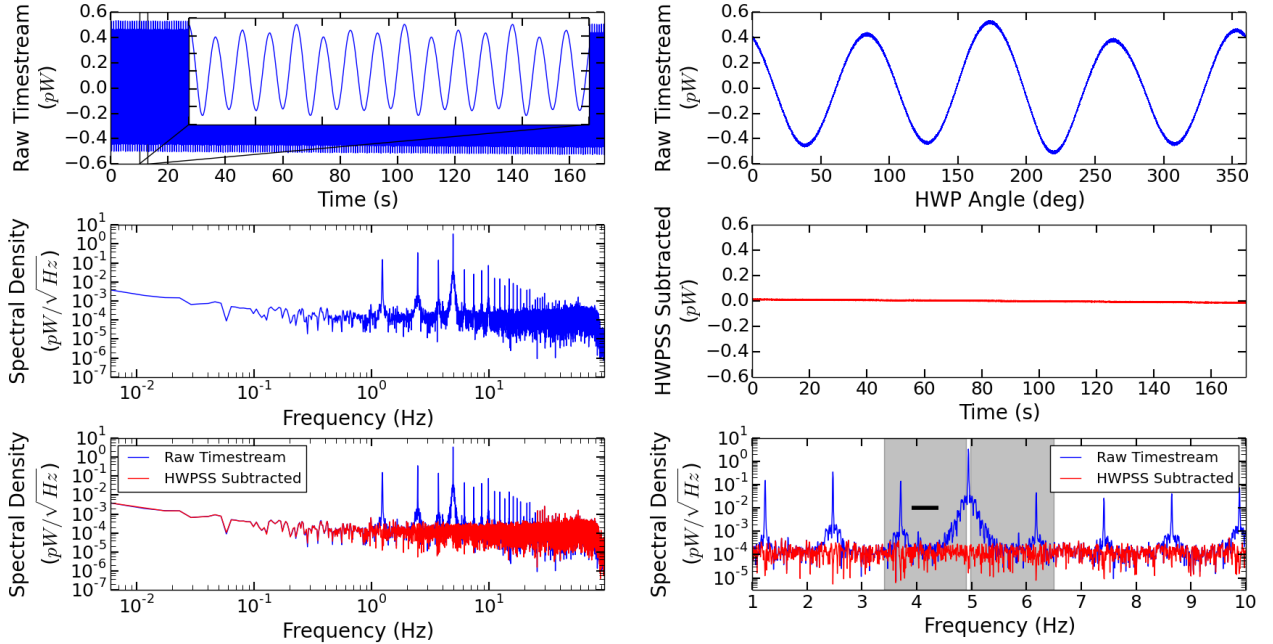


Fig. 3.— Time ordered and spectral density data for 172 s section of a 150 GHz detector before (blue) and after (red) HWPSS removal. The TOD are given in units of power incident on the telescope. For the 150 GHz band, 0.31 pW power fluctuation is equivalent to 1 K_{CMB} . Upper left: calibrated time domain data and a magnified view of 3 s (inset) showing a sinusoidal behavior in time. Upper right: the data in HWP angle demonstrating a stable signal that is synchronous with the rotation of the HWP. Middle left: spectral density of the data. Middle right: the data (upper left) after subtraction of the HWPSS. Lower left: spectral densities before and after HWPSS removal. Lower right: spectral densities before and after HWPSS removal on a linear frequency scale, showing the first eight harmonics of the HWP rotation frequency. The shaded region indicates the sidebands surrounding the fourth harmonic, in which the Q and U signal reside. The black bar indicates the frequency range (from 3.9 to 4.4 Hz) used to quantify noise levels.

In this paper we give an assessment of the noise properties of the instrument including during astrophysical observations. To assess these noise properties we first removed the HWPSS. The HWPSS is modeled as the sum of the first 20 harmonics of the HWP rotation frequency. The HWPSS for a given detector is estimated by performing a maximum likelihood fit of the sine and cosine amplitudes of the harmonics on 60 s chunks of data. In addition to a constant term, the amplitudes are also allowed to vary linearly with time. This procedure follows the one used for MAXIPOL (Johnson et al. 2007) and more details are given in Didier (2016) and in Araujo (2017). The HWPSS is subtracted from the raw detector timestream to yield the “HWPSS-subtracted” timestream. When we quote noise properties we give special attention to a narrow band of frequencies between 3.9 and 4.4 Hz. This band is within the side-band of the 4th harmonic of the HWP rotation which contains half of the Stokes Q and U sky synchronous signals. (The other half is contained in a symmetric side-band placed above the 4th harmonic.)

Analysis of data collected throughout flight showed that the amplitude of the HWPSS was sufficiently large to introduce a non-linear detector response. (A similar effect was observed by the Polarbear team (Takakura et al. 2017).) EP4 discusses this non-linear response and a technique to mitigate its effects.

4. Readout

The TES bolometers were voltage biased (Lee et al. 1998). Incident optical power fluctuations modulated the current across the bolometer and across a series inductor and capacitor. A SQUID transimpedance pre-amplifier converted the modulated current to a voltage signal that was subsequently further amplified, digitized, and filtered (Yoon et al. 2001).

We used frequency domain multiplexing (FDM) to couple several detectors to a bias and a readout line (Yoon et al. 2001). When the EBEX program began, power dissipation of state-of-the-art analog FDM readout boards consumed approximately 5 W per readout channel, giving a total consumption of nearly 10 kW, a prohibitive level for a balloon-borne payload. We have therefore embarked on implementing a new digital frequency domain multiplexer (DfMUX) scheme that had approximately one tenth the power consumption (Dobbs et al. 2008). EBEX was the first experiment to implement this scheme, multiplexing 8 detectors with two wires in its 2009 engineering flight, and the first to multiplex 16 detectors in its EBEX2013 flight.

The EBEX readout system required investment of effort along three dimensions: development and testing of the new DfMUX electronic boards, the development of automated on-board software to bias and read the TES bolometers and the SQUID pre-amplifiers, and the development and implementation of a cooling system that dissipated the 593 W consumed by the DfMUX boards. We discuss only the first element in this section. The software and cooling system are discussed in EP3. Aubin et al. (2010), Aubin (2012), MacDermid et al. (2014), and MacDermid (2014) give more details about the EBEX readout system.

4.1. Superconducting Broad-side Coupled Microstrips

During operation the EBEX TESs had a resistance of approximately $1\ \Omega$. Stray impedance in series with this resistance reduces the detector’s voltage bias and causes crosstalk. Therefore we kept the bias and readout wires between the SQUIDs and the LC boards superconducting. Some sections of the wiring were commercially made, but for the longest sections we designed and constructed superconducting broad-side coupled microstrips (Polsgrove 2009; Dobbs et al. 2012).

The microstrips consisted of interleaved layers of kapton and niobium-titanium wires. We selected niobium-titanium because it has a critical temperature of 9.2 K and low thermal conductance in the superconducting state. We chose a parallel-plate waveguide geometry to minimize stray inductance; see Figure 4. We fabricated the flat niobium-titanium wire from 191 μm diameter niobium-titanium wire which was copper-clad¹ to a total diameter of 305 μm and rolled flat² to thickness of about 33 μm . We dissolved the copper-cladding from the entire length of the flattened wire except for the ends using a nitric acid wash. The copper-cladding remaining at the ends was used to facilitate soldering the wires. The final cross-sectional dimensions of the wires are 760 by 33 μm . To electrically isolate the two wires in each pair, a film of 7.6 μm thick Kapton HN was used as a spacing layer. Adjacent pairs were spaced apart by 940 μm and were secured in their position by a layer of 64 μm thick Kapton HN tape with silicone adhesive. Each microstrip had 8 pairs of wires. We measured inductances of 24.5 and 33.3 nH for the 70 and 95 cm EBEX microstrips, respectively.

For each microstrip the ends of the wires were soldered to small flexible circuit boards that had a micro-D connector. The micro-D connectors mated the microstrips to the SQUID boards on one end, and to the LC boards on the other. The microstrips were coupled to the SQUID and LC boards with 4 connectors. We calculated an inductance of 9 nH per connector giving an estimated total stray inductance of 60.5 and 69 nH for the two lengths. In EP1 we describe the ‘RF tower’ assembly through which the microstrips passed between these two sets of boards. The RF tower gave heat sinking for the microstrips and was part of the RF protection of the receiver.

4.2. Digital Frequency Domain Multiplexing

The EBEX detectors were read out with the DfMUX readout system described in Dobbs et al. (2008). A schematic diagram is shown in Figure 5. For the EBEX2013 flight we implemented a multiplexing factor of 16 (Aubin 2012), the highest used at the time with this readout approach. Ceramic capacitor C_i in series with 24 μH inductors L and the detectors, which had resistance R_i , defined resonant frequencies f_i between 200 and 1200 kHz. The detectors were voltage biased with a 30 m Ω resistor R_{bias} and their output current was nulled to reduce dynamic range requirements. The SQUIDs (Huber et al. 2001) were operated in a shunt-feedback with a low-noise transistor op-amp and a feedback resistor R_{FB} of 5 k Ω located on a custom SQUID controller circuit board (Lanting

¹Supercon, Inc.

²H. Cross Company

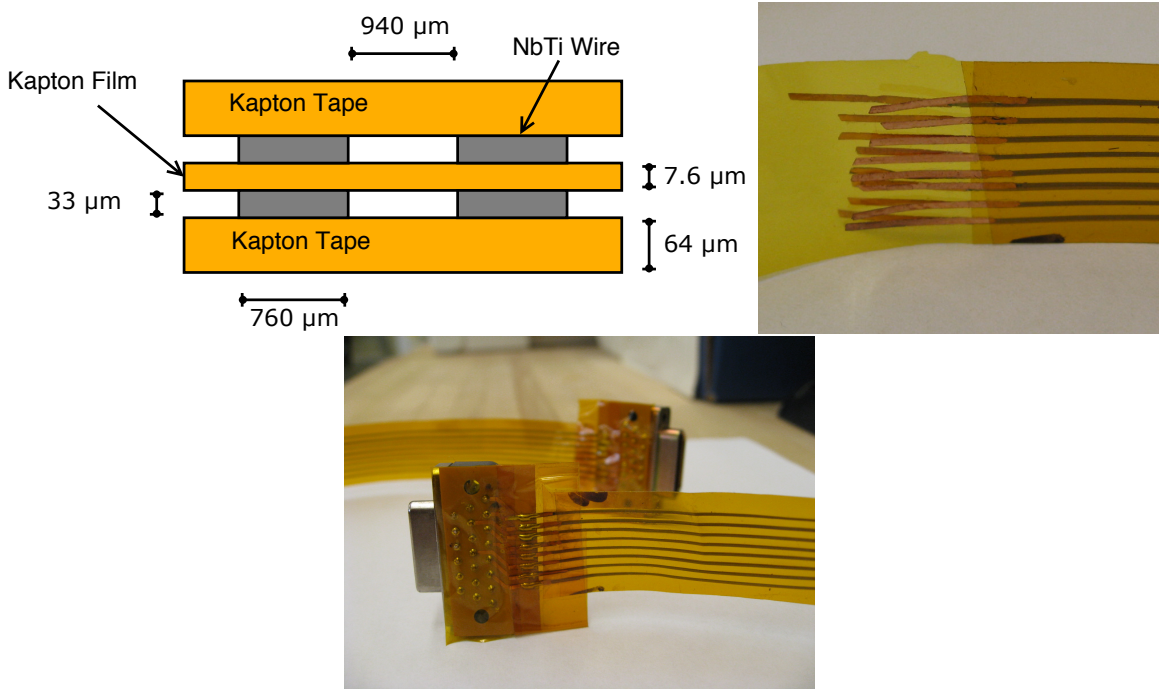


Fig. 4.— Upper left: diagram of the cross-section of the microstrip geometry. Two of the 8 pairs of wires are shown. Upper right: image of copper-clad niobium-titanium wire ends. Lower panel: image of the microstrip soldered to micro-D connectors.

2006). The wires between the SQUIDs and the room temperature SQUID controller boards were constrained to be shorter than 33 cm (Dobbs et al. 2008). For longer wire lengths, the phase of the signal shifted by more than 45° giving positive instead of negative feedback. For EBEX the length of these wires³ was 19.5 cm. The amplified output bolometer currents were digitized at 25 MHz, demodulated, filtered, and decimated to 190.73 Hz by the field programmable gate array (FPGA)⁴. The data were packetized by a Microblaze virtual processor which was part of the FPGA and were streamed to the flight control computer over Ethernet for storage, as described in EP3.

We operated 28 DfMUX readout boards and 112 SQUIDs during the EBEX2013 flight. Each board provided biases to and read out 4 SQUIDs and therefore 64 detectors. The boards were separated into four bolometer readout crates (BRC) each containing either 6 or 8 boards. In addition to the readout boards, each BRC had a VME backplane, a clock distribution board, and an ethernet communication ring switch. One of the BRCs also held boards that were used to cycle the sub-kelvin refrigerators and read out receiver temperatures. The clock distribution board distributed the 25 MHz clock signal, as well as the commands to turn on/off the boards, and the commands that triggered the re-programming of the boards' firmware. Each BRC shell acted as a Faraday cage, shielding the readout electronics from RF signals. Two other electronic crates each

³Tekdata Interconnections Limited

⁴Xilinx Virtex-4 FPGA

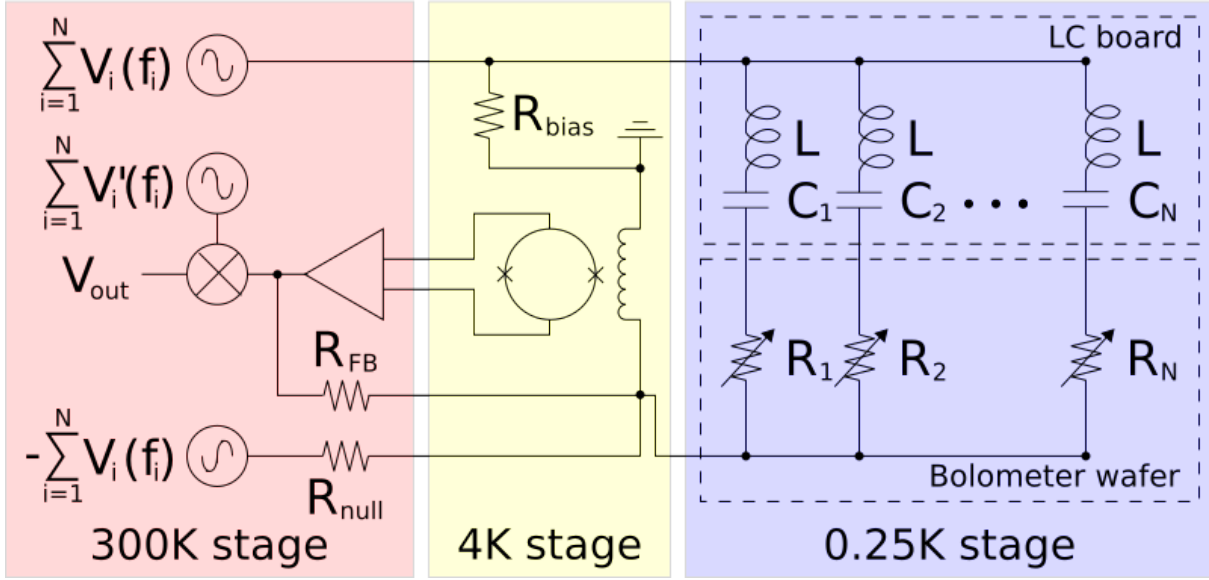


Fig. 5.— Schematic of the frequency domain readout system following Aubin (2012). Colors encode different temperature stages. For the engineering flight N was 8; for the EBEX2013 flight N was 16.

populated with DC/DCs⁵ converted unregulated 28 V to regulated 6 and 10 V (Sagiv 2011; Sagiv et al. 2012). Each crate supplied 296 W to two BRCs; this is 21 W per DfMUX board or 0.33 W per readout channel. Factoring in the 82% efficiency of the DC/DC the total power consumption of the readout system was 723 W.

The DfMUX on-board ‘algorithm manager’ software listened for JavaScript Object Notation (JSON) formatted requests over TCP/IP issued by the flight control computer via Ethernet communication and executed the requested Python-coded task. The virtual processor of each DfMUX board was programmed to perform tasks in parallel on up to two SQUIDs or the 32 detectors wired to them. These tasks were stored on the DfMUX board flash memory and included tuning the SQUIDs, configuring the voltage biases for the detectors, and ensuring the SQUIDs were operated within their dynamic range (see more details in MacDermid et al. (2009)). With this architecture we parallelized the array tuning process saving observing time and reducing the load on the flight control computer. Since each DfMUX board operated four SQUIDs and could perform up to two tasks in parallel, tuning time of the detector array was equivalent to the time to tune two SQUIDs and their associated 32 detectors, and was independent of the total number of detectors populating the focal plane. Once the task was completed, the result was sent back to the flight control computer through Ethernet for storage. The interaction between the DfMUX boards and the flight control computer is further described in EP3.

⁵Interpoint Series from Crane Aerospace and Electronics

4.3. Readout System Noise and Stability

4.3.1. Noise

The term ‘readout noise’ refers to noise contributions from the SQUID pre-amplifier and the electronic components of the readout system. It excludes the contributions from the detectors which are described in Section 5.5. The performance of ‘dark SQUIDs’ and resistor channels inform the readout noise level independent of detector noise contributions. Unless otherwise noted, we refer to data that was collected during flight. The data was converted from raw digital units (counts) to current through the SQUID by applying the measured transfer function of the readout system dI_b^A/dI_b^c (Aubin 2012)

$$X \text{ [A}/\sqrt{\text{Hz}}] = X \text{ [counts}/\sqrt{\text{Hz}}] \cdot dI_b^A/dI_b^c \text{ [A/count]}. \quad (1)$$

The process to generate noise predictions, which are compared to measurements, is described in Aubin et al. (2010) and in Aubin (2012). We also include a ‘current sharing’ noise term that is not described in these publications. This noise term arises because current driven through the SQUID feedback wire is shared between the SQUID input coil and the bolometer. Noise sources originating downstream of the SQUID but inside the feedback loop will result in a feedback current that is enhanced by this sharing. The negative feedback will increase the current, enhancing the noise from these sources (Silva-Feaver et al. 2017). Current sharing depends on the relative size of the SQUID input reactance and the bolometer impedance. To calculate the effect for noise expectations, we use a measurement of the SQUID input inductance for the same SQUID model implemented in a different instrument, ~ 350 nH, and include it in our noise expectations (Silva-Feaver et al. 2017).

A dark SQUID is a SQUID whose input coil was not connected to detectors or to the sub-kelvin LC boards. Generally, the input wires for a dark SQUID are left open (unterminated) at the 4 K stage; see Figure 5. We demodulated each of the two dark SQUIDs at 16 frequencies within the 200 - 1200 kHz range typically used to bias detectors. We similarly demodulated two other SQUIDs which became inadvertently dark when they developed an electrical open wire once cooled to 4 K. The current spectral density through the SQUID input coil of a typical dark SQUID for 172 s of data is shown in Figure 6. Median predicted noise contributions for the 64 channels are given in Table 1. The ratio of average measured to predicted noise between 1 and 10 Hz for the SQUID channel in Figure 6 is 1.2, which we consider to be broadly consistent with expectations from Table 1, given uncertainties in the transfer functions, component values, and SQUID noise. We use a relatively broad bandwidth to average the noise because we find no evidence for the HWPSS signal with the dark SQUIDs. This noise level is reasonably stable over the entire flight. We show data spanning 18 hours in Figure 6.

To quantify the readout noise over the entire flight and for all dark SQUIDs we calculated power spectral densities for 172 s section of data every 20 min throughout flight. We found the median measured-to-predicted ratios throughout flight for a given dark SQUID channel. We histogrammed all the channel medians and extracted a single median value representing the performance of the 64 dark SQUID channels; see Figure 7. The 48 well behaved channels had a median value of 1.2 when the noise is averaged between 1 and 10 Hz. One dark SQUID showed ratios larger than 4 for all

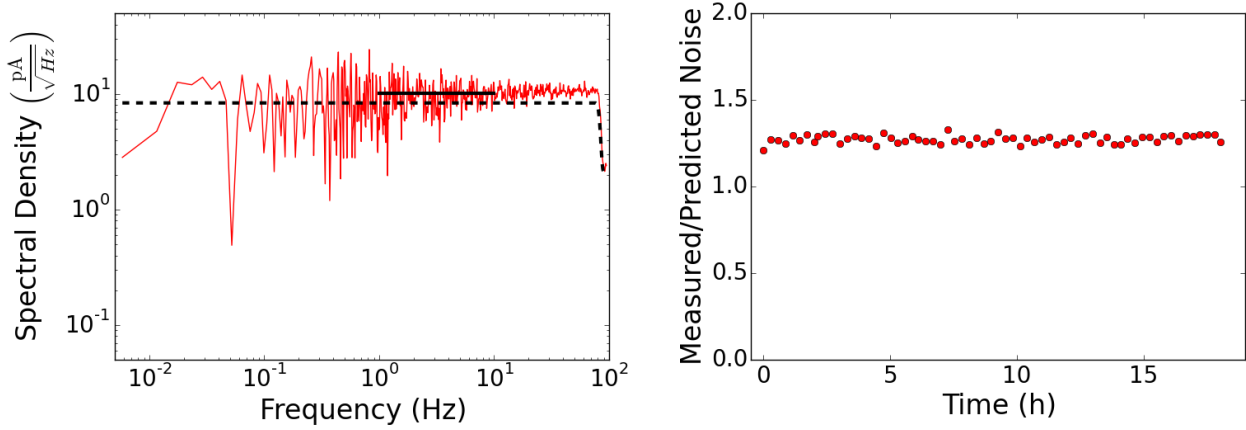


Fig. 6.— Left: the current spectral density of a dark SQUID channel demodulated at 495 kHz. The average level between 1 and 10 Hz (solid red) is $10 \text{ pA}/\sqrt{\text{Hz}}$. The predicted level (dashed line) is $8.4 \text{ pA}/\sqrt{\text{Hz}}$. Right: the ratio of measured-to-predicted noise as a function of time for the same channel.

Noise source	Value $\text{pA}/\sqrt{\text{Hz}}$
SQUID	$\sqrt{2} \cdot 3.5$
Demodulation chain	$\sqrt{2} \cdot 3.8$
Nuller chain	$\sqrt{2} \cdot 2.4$
Total	$\sqrt{2} \cdot 5.7$

Table 1: Components of the predicted post-demodulation noise for dark SQUIDs. SQUID noise of $3.5 \text{ pA}/\sqrt{\text{Hz}}$ is typical for our devices (NIST 2010). The explicit factors of $\sqrt{2}$ are due to uncorrelated power on both sides of the demodulation frequency. The nuller chain noise is dominated by resistor Johnson when not providing nulling currents.

of its channels and is considered an aberration. This high-noise SQUID was connected to detector modules but exhibited an open connection in one of its two input wires. We speculate the other wire acts as a high impedance antenna, coupling unwanted EMI into the SQUID input resulting in high noise.

We also found a consistent median ratio of 1.2 when using measurements on the launch pad, just before flight. Similar measurements performed in two different test cryostats with different SQUIDs gave nominal noise levels suggesting that the 20% higher median ratio could have a contribution from environmental pickup, differences in the SQUIDs, or signals coupled from elsewhere in the instrument. A $\sim 5\%$ variation is measured between the lowest and highest frequency channels which is likely caused by the omission of stray inductance in the noise prediction.

Resistor channels had the entire readout chain coupled to 1Ω resistors that were mounted on the

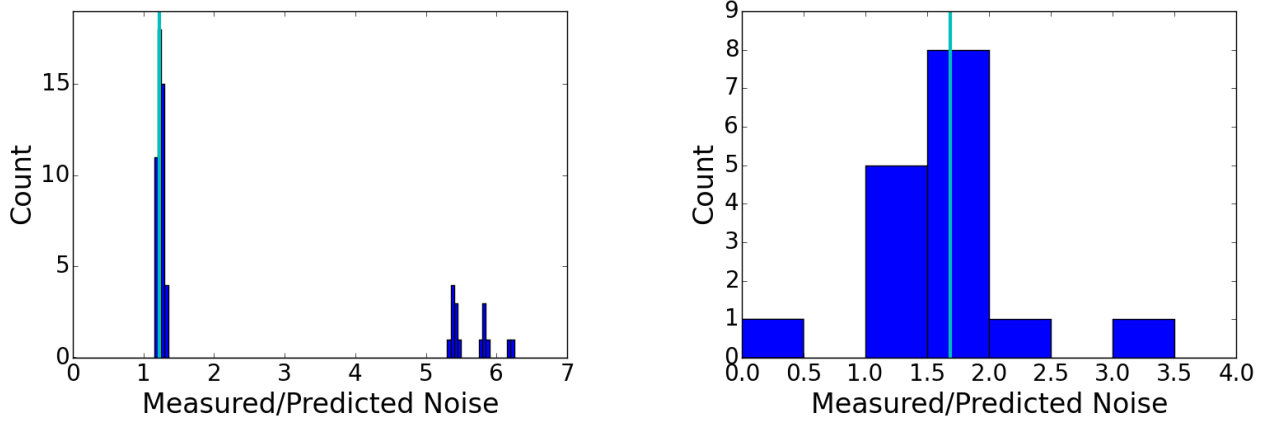


Fig. 7.— Left: the distribution of measured-to-predicted noise ratio for the 64 dark SQUID channels. The median for the 48 well-behaved channels (vertical cyan) is 1.2. Right: the distribution of measured-to-predicted noise ratio for the 16 resistor channels. The median (vertical cyan) is 1.7.

LC boards. The noise for the resistor channels consists of both Johnson and readout noise terms. The total noise with these channels represents a cross-check on measurements of the detectors’ noise when they were biased above their superconducting transition, as discussed in Section 5.5. The analysis of the data parallels that of the dark SQUIDs. Figure 7 shows the distribution of the median measured-to-predicted noise ratio for 16 well-behaved resistor channels throughout flight; 5 additional resistor channels had a noise ratio more than 3.5 times the median and were excluded from the analysis. The resistor channels have a median measured-to-predicted noise ratio of 1.7. The resistors are mounted on the 0.25 K stage. We hypothesize that wires of 70 - 95 cm long from the SQUIDs act as antennas allowing electro-magnetic pickup to couple to the SQUID input, producing excess noise. Coupling such as this can produce narrow-band features in noise spectra if the EMI lies in the carrier bandwidth, resulting in detector-by-detector variations, or broadband white noise if the EMI is away from the carrier bandwidth but coupled to the SQUID. Another potential increase in noise is another detector, or detectors, sharing the same SQUID and thus the bias lines for same comb of frequencies. For example, a ‘latched’ detector - a detector operating below the superconducting temperature - increases the noise level for all other readout channels on the same comb.

After the EBEX North American engineering flight noise was measured in the laboratory with detectors above the superconducting transition. As we discuss in more detail in Section 5.5.1, in terms of readout-chain noise expectations, this configuration is similar to the resistor channel setup for the science flight. The ratio of measured to predicted noise was 1.0 ± 0.1 (Aubin et al. 2010), which suggests that the excess resistor noise measured in the science flight is an environmental effect, rather than inherent to the readout chain. We revisit and discuss this again in Section 5.5.1.

We find no evidence for correlated noise between the data of any of the dark channels. Using 18 contiguous time sections, 86 s each, we calculate the coherence of all pairs of channels. We

compare the average coherence between all pairs to the expectation for white noise, which with our data is 0.17. We find a coherence of 0.16 with a dispersion of 0.01 for dark SQUIDs and 0.2 with a dispersion of 0.1 for resistor channels.

4.3.2. Gain Variations

We monitored gain fluctuations of the readout system by using 24 unused readout channels distributed over 12 SQUIDs, which also read out live detector channels, a pair per SQUID. For these channels, no biases were supplied through the carrier wire since they are operated far from any LC resonance in the cold multiplexer; see Figure 5. Instead, we injected two small constant sinusoidal currents, one at 110 kHz and the other at 1,260 kHz, into the input coil of the SQUID using the nuller wire. These frequencies were 60 kHz above and below our standard lowest and highest bias frequencies. The amplitudes were either 30 or 100 nA. The signals were demodulated at a frequency 9 Hz higher than the nulling current resulting in a 9 Hz demodulated sinusoidal current; see Figure 8. These data were then processed like all other bolometer data.

Since the injected current was constant, amplitude modulation of the demodulated signal is an indication of readout gain variation. The variation of gain for one channel over 12.7 hours of flight is shown in Figure 8. This particular channel experiences a gain change of 0.25%. The data points are from 85.9 s sections of data separated by 10 minutes. A histogram for all gain monitoring channels gives a stability that is mostly better than 1%. Over the same period of time temperature sensors on the readout boards indicate board temperature changes of up to 20°C. We measure in the laboratory that a similar temperature change of one readout board causes its gain to change by up to 0.3%. We conclude that gain variations of the readout system are negligible compared to the overall calibration uncertainty, which is $\gtrsim 10\%$.

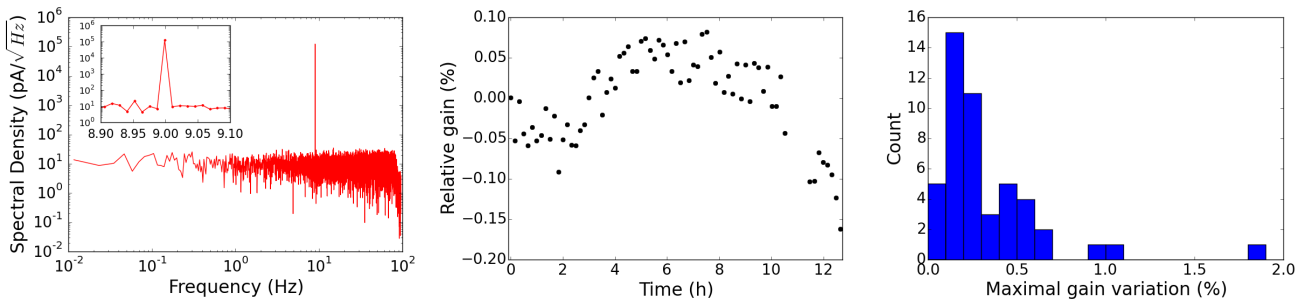


Fig. 8.— Left: current spectral density for one gain-monitor channel. The sharp line at 9 Hz is the demodulated nuller current provided to the SQUID coil at 110 kHz and demodulated at 110 kHz + 9 Hz. Middle: the time variation of the readout gain for one channel during 12.7 hours. The maximal peak-to-peak gain variation is 0.25%, which is negligible compared to the overall calibration uncertainty. Right: the distribution of the maximal gain variation measured at 2 frequencies for 12 SQUIDs for multiple segments of the EBEX2013 flight.

5. Detectors

EBEX uses spider-web TES bolometers. We optimized the parameters of the bolometers for cosmological observation from a balloon platform. In this section we describe the design characteristics of the EBEX bolometers and report on measurements of their normal resistance, thermal conductance, critical temperature, time constant, and optical efficiency. We use these measurements in combination with the measured absorbed power by the detectors to predict the noise performance of the detectors. We finally compare these predictions to data to assess their in-flight performance.

5.1. Detector Design

The detectors had spider-web absorber architecture similar to the TESs used for the APEX-SZ and SPT-SZ experiments (Lee et al. 1996; Chang et al. 2009; Schwan et al. 2011; Westbrook et al. 2012; Westbrook 2014). The design of a single TES, shown in Figure 9, consisted of a low-stress silicon nitride, gold-metalized web that served as the absorber for millimeter-wave radiation. The web was suspended above the silicon wafer by 8 legs, which provided thermal isolation, and were used to tune the thermal conductance of the bolometers. A TES made of aluminum-titanium superconducting proximity bilayer in the middle of the web was operated at its transition temperature, typically between 0.4 and 0.5 K. Two niobium leads delivered constant voltage bias and monitored current fluctuations.

Table 2 gives the bolometer design parameters for the three EBEX frequency bands, including the TES electrical resistance in the normal state (R_n), TES transition temperature (T_c), average thermal conductance (\bar{G}), bolometer geometry parameters α and β described in Figure 9, the expected heat capacity (C) of the bolometers, and the intrinsic optical time constant (τ_0). The choice of some of the design parameters, most notably the thermal conductance, reflects the unique demands of a balloon flight; the in-flight optical loading is not a-priori known, and once the instrument is conducting observations there is no opportunity for further detector optimization. Therefore the thermal conductance must have sufficient margin, that is, must be large enough, to ensure the detectors can operate over a relatively broad range of optical loadings. A consequence is that with nominal optical load a larger detector voltage bias is required, which reduces the responsivity and amplifies readout noise equivalent power.

5.1.1. TES, Absorber, and Backshort

The TESs were constructed from a 110 nm titanium layer deposited on top of a 40 nm aluminum layer in a single vacuum step. We chose a transition temperature of 0.44 K to minimize phonon noise given the expected 0.25 K focal plane temperature (Suzuki 2013). The normal resistance for all bands was $1.5\ \Omega$ to ensure that the detector operated in the stable regime (Dobbs et al. 2012).

A metalized spiderweb structure appears as a continuous sheet of metal with resistivity ρ_{web} to electromagnetic radiation of wavelength λ incident upon it as long as the grid spacing g satisfies

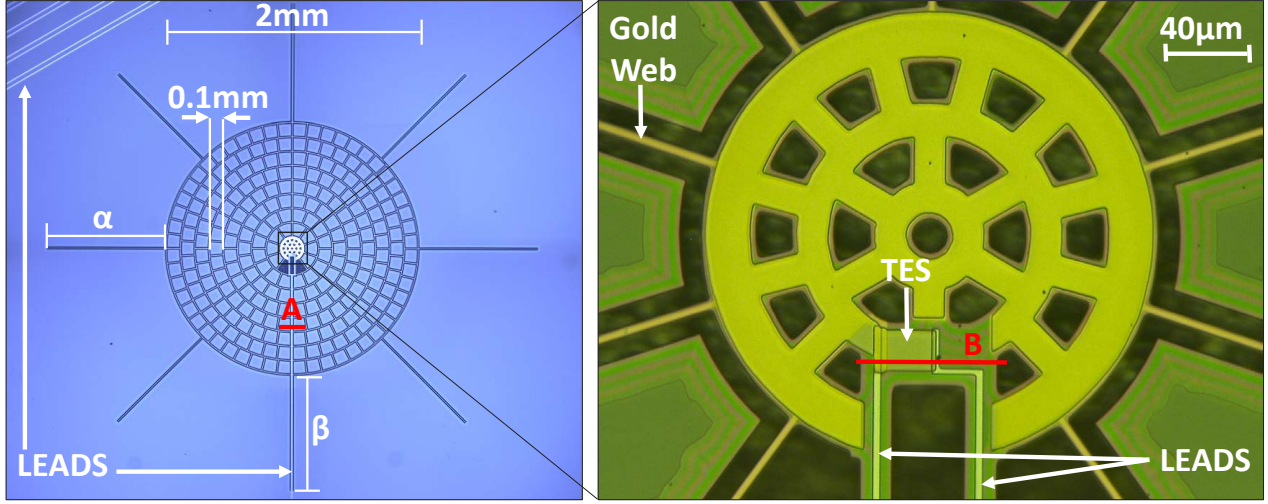


Fig. 9.— Left: photograph of an EBEX bolometer. Right: an enlargement of its central region. The leg with length β was 17 μm wide to accommodate the niobium leads. The other 7 legs (with length α) were 6 μm wide. Table 2 gives the dimensions of the parameters α and β . Red lines labeled “A” and “B” indicate cross-sections which are shown in Figure 10.

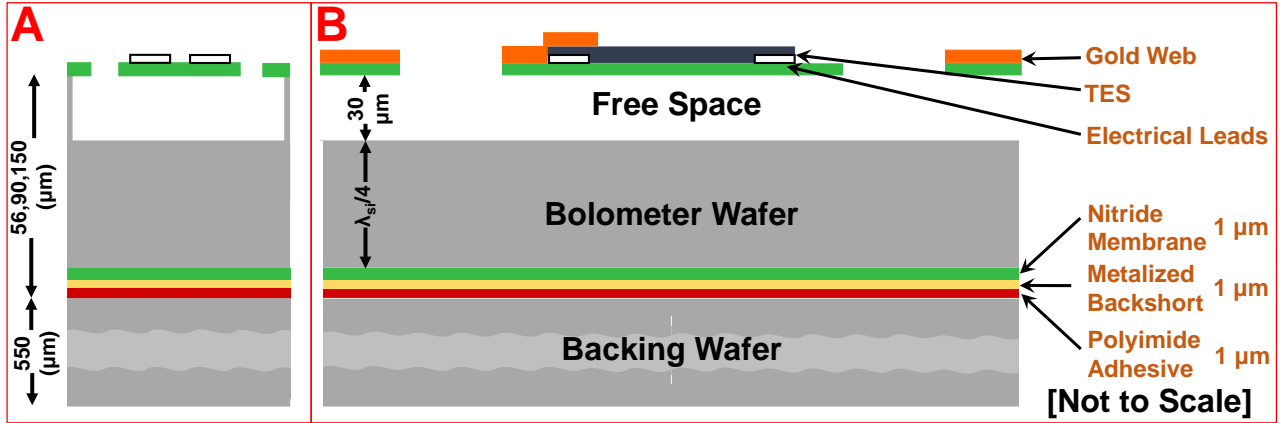


Fig. 10.— Cross-sections through the lines “A” and “B” from Figure 9 showing the layers of the EBEX detectors through the thermal isolation leg carrying the electrical leads (A) and the central portion of the bolometer which carries the TES (B). The thickness of bolometer wafer depended on frequency band; see text. The bolometer wafer was bonded to a thicker backing wafer to provide mechanical stability during fabrication. A metallic layer deposited on the backside of the detector wafer provided a backshort for increased absorption. An aluminum-titanium bilayer forms the TES of the bolometer at the center of the pixel.

$g \ll \lambda$ (Bock et al. 1995). In addition, the return loss remains below -10 dB when ρ_{web} is between 150 and 700 Ω/sq (Glenn et al. 2002). The EBEX web grid spacing was 100 μm , 7 times smaller than the shortest wavelength admitted, and we used 200 \AA thick layer of gold to achieve $\rho_{web} = 350 \Omega/\text{sq}$.

The absorption efficiency of the detector depends on the distance of the backshort from the absorber. Within a single uniform silicon medium the optimal distance is $\lambda_c/4$, where λ_c is the

Band (GHz)	150		250		410	
	Design	Measured	Design	Measured	Design	Measured
R_n (Ω)	1.5	1.9	1.5	1.5	1.5	1.4
T_c (K) [‡]	0.44	0.45	0.44	0.48	0.44	0.47
\overline{G} (pW/K)	19	39	45	54	63	63
τ_0 (ms)	17	88 [†]	13	46 [†]	10	57 [†]
C (pJ/K)*	0.5	3.8 [†]	0.9	3.3 [†]	1.0	8.4 [†]
Wafer thickness (μm)	150		90		56	
α (mm)	1.05		1.0		0.5	
β (mm)	1.45		1.0		0.5	

[‡] Design values calculated early in the program using thermal conductivity power index $n=3$ and a bath temperature of 260 mK.

[†] Median of measurements on a single wafer at each frequency; see Section 5.2.4.

* Calculated from time constant and thermal conductance.

Table 2: Designed and measured detector parameters for each of the frequency bands. The values in the ‘measured’ columns are median values for all detectors on wafers used for flight. Description of the measurements and histograms and further discussion of the measured values are given in Section 5.2. For the parameters α and β shown in Figure 9 we give the design values. The lithography was generally accurate to within $0.5 \mu\text{m}$.

wavelength in solid silicon behind the web absorber; $\lambda_c = \lambda_0/n_{Si}$, where λ_0 is the wavelength in empty space and $n_{Si} = 3.4$ is the index of refraction of silicon (Lamb 1996; Phillips & Zmuidzinas 2003). To achieve these backshort thicknesses we etched the detector wafers to thicknesses of 150, 90, and $56 \mu\text{m}$ for the 150, 250, and 410 GHz bands, respectively. However, these wafer thicknesses were too thin to survive standard micro-fabrication techniques and we thus bonded the bolometer wafer to a thicker backing wafer to provide additional mechanical stability (Westbrook et al. 2012; Westbrook 2014); see Figure 10.

When we include in the absorption simulation the $30 \mu\text{m}$ cavity behind the web absorber, which makes the backshort a combination of two media, we find that the expected absorption efficiency of the 410 GHz is 35% and is 75% for the other two bands.

5.1.2. Thermal Conductance

Table 2 gives our specifications for the average thermal conductance for each of the frequency bands. We arrived at these specifications by conservatively requiring that the bolometer handle total absorbed powers of up to 4, 9 and 12 pW for each of the 150, 250, and 410 GHz bands, respectively, before the TES exits the superconducting transition. We set these requirements early in the development of instrument by calculating the expected optical loads from both sky and instrument sources and by applying a safety factor to account for unexpected loads. We find that our conservative specifications are met when comparing to the measurement of the in-flight total optical load described in Section 5.3.

Of the two contributions to the thermal conductance of the bolometer, (i) the silicon nitride legs that connected the web to the wafer, and (ii) the two niobium electrical leads, the thermal conductance of the niobium leads was negligible (Kes et al. 1974; Westbrook 2014). Therefore, we achieved different thermal conductances for each frequency band through changes in the geometry of the silicon nitride legs. The geometry of the legs and the calculated average thermal conductances are given in Figure 9 and in Table 2.

5.1.3. Intrinsic Time Constant

The intrinsic optical time constant of the bolometer τ_0 is set by the ratio of the heat capacity C at the operating temperature to the dynamic thermal conductance $G = dP/dT$: $\tau_0 = C/G$. The predicted heat capacity of the bolometer was dominated by the contributions of the TES and the gold absorber layer, which gave 80% and 20% of the total, respectively. The calculated contributions of the silicon nitride web and niobium leads were calculated to be negligible (Westbrook 2014; Van Sciver 2012). Since the TES and gold layer were identical among the frequency bands, changes in the time constant with frequency band were a result of differences in thermal conductance. Table 2 gives the design values of τ_0 for each of the frequency bands. The table quotes the average thermal conductance \overline{G} , which is related to the dynamic value through

$$G = (n + 1) \left(\frac{1 - \left(\frac{T_0}{T_c}\right)}{1 - \left(\frac{T_0}{T_c}\right)^{n+1}} \right) \overline{G}, \quad (2)$$

where T_0 is the bolometer bath temperature and thermal conductivity is assumed to follow a power law, $\kappa = \kappa_0 T^n$ (Irwin & Hilton 2005). We used $n = 2$ since thermal conductivity measurements of engineering flight wafers gave values of 2.2 ± 0.3 , 1.9 ± 0.2 , and 2.1 ± 0.2 for the 150, 250, and 410 GHz bands, respectively (Hubmayr 2009; Aubin et al. 2010).

5.2. Detector Characterization

We characterized the properties of all 14 detector wafers that were included in the EBEX2013 flight. Characterization included testing for electrical continuity of each detector before a wafer was wire-bonded with an LC board and a standard set of measurements at cryogenic temperatures in dark conditions. In dark conditions, the wafer was mounted inside a sealed box cooled to 0.32 K and thus was subjected to an optical power load of ~ 9 fW, which is two orders of magnitude smaller than expected in-flight conditions.

There were 140 bolometers fabricated on a single EBEX wafer, of which we could read out 124 with the edge, and 127 with the central, LC boards. This gave a total of 1960 bolometers from which 1742 could be read out, as listed in the first two lines of Table 3. We now enumerate further reductions in detector yield. At room temperature, each bolometer was inspected visually under a microscope and also probed across its bond pads for electrical continuity (line 3). To monitor noise, some electronic channels read out resistors located on the LC boards (two per wafer), four combs

were attached to dark SQUIDs that did not have bolometers, and one SQUID had an electronic malfunction (line 4). Some bolometers which had electrical continuity at room temperature did not have continuity during the cold (0.8 K) network analysis (line 5). Of the 112 SQUIDs 5 failed to tune (line 6). Those bolometers whose operation drastically worsened the noise performance of their entire comb were disconnected (line 7). The number of bolometers that had successful IV curves during first tuning at float is given in line 8.

	Count of	Frequency (GHz)			Total
		150	250	410	
1	detectors on wafers	1120	560	280	1960
2	maximum detectors to read out	992	496	254	1742
3	detectors which passed warm electrical & visual inspections	908	455	232	1595
4	channels wired to detectors which passed warm electrical & visual inspections	861	447	213	1521
5	detectors which passed the 0.8 K network analysis test	805	430	187	1422
6	detectors after SQUID failures removed	773	414	155	1342
7	detectors after noise polluters removed	676	371	133	1180
8	detectors with successful flight IV curves	504	342	109	955

Table 3: Detector yield tally by frequency band.

5.2.1. Resonant Frequencies

We determined the resonant frequencies for each comb of frequencies by maintaining the detectors at 0.8 K, that is, above their transition temperature, and sweeping the bias frequencies between 0.1 and 1.3 MHz. The RLC circuit resonated at its characteristic frequency such that the entire sweep gave a response as shown in Figure 11. A fit of the peak of the resonance with a model of the circuit that accounts for current leakage to all resonators gave the resonant frequencies and the normal resistances of the TESs in the comb (Aubin 2012). Missing peaks in this measurement corresponded to opens in electrical lines.

Figure 12 gives histograms of the measured normal resistance R_n values for each frequency band. The 150 and 410 GHz bimodal distributions were due to detector parameters being closely grouped within a single fabrication run, but varying between fabrication runs. The measured value of R_n for the 250 GHz band closely matched the design (see Table 2). For the other two frequency bands, one mode of the distribution closely matched while the other mode was higher (lower) than design for the 150 (410) GHz band. The 150 GHz detectors with a measured R_n of 1.9 Ω , instead of the nominal 1.5 Ω , were calculated to have increased electrical cross-talk from a value of 0.5% to 0.8% and decreased loopgain by 30%. The 410 GHz detectors with a measured R_n of 1.4 Ω were calculated to have increased Johnson noise by 4% relative to the nominal expected value of 4.0 pA / $\sqrt{\text{Hz}}$.

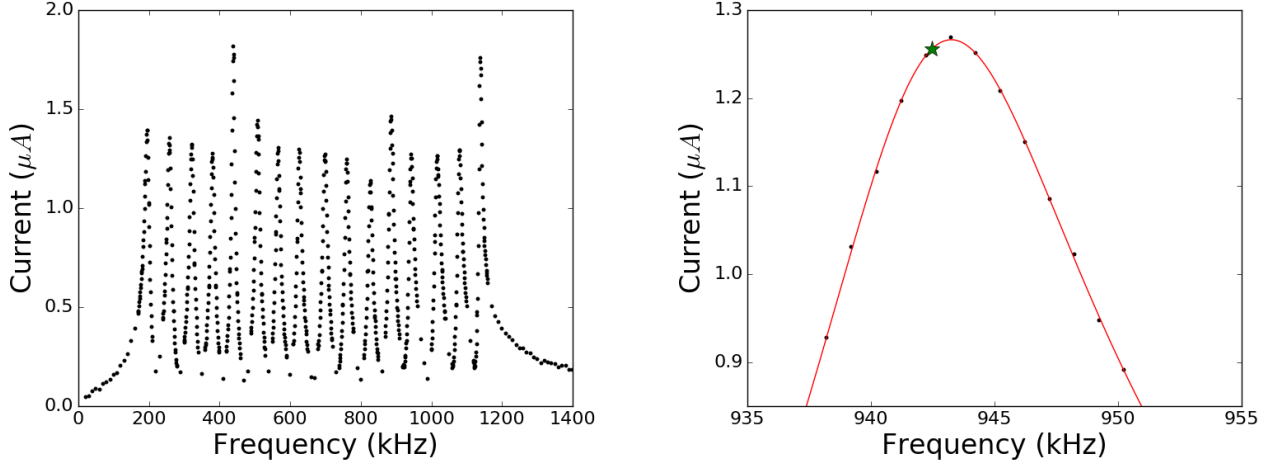


Fig. 11.— Left: current response of a multiplexed detector circuit as a function of bias frequency. Right: zoom on one peak (black dots) with the fitted response (red line) and the optimal bias frequency (green star) minimizing crosstalk (Aubin 2012).

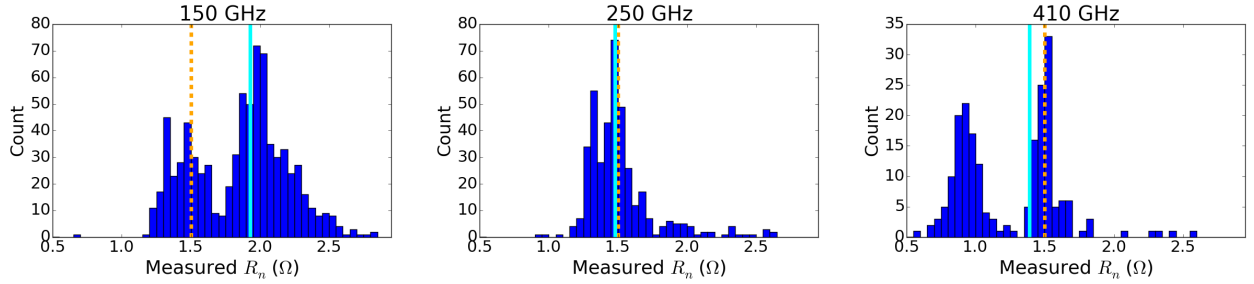


Fig. 12.— Histogram of measured normal resistances R_n for each of the frequency bands, including the median (vertical cyan) and design (vertical gold dashed) values.

5.2.2. Transition Temperature

For the measurement of the critical temperature T_c we biased the detectors with 5 nV such that the Joule heating of 1.5 fW was small and the bath temperature was a good proxy for the bolometer’s temperature. For the same reason, the measurement was done in dark conditions. We slowly changed the detectors’ temperature while monitoring the current through the TES. At the critical temperature the current showed a steep transition. Figure 13 shows histograms summarizing the measured critical temperatures. There was a $\sim 20\%$ wafer-to-wafer spread in the measured T_c with the medians for the three bands within 11% of the target value of 0.44 K. The 150 GHz detectors have the widest spread of measured T_c . The effect of this spread is twofold: (1) it increases Johnson (phonon) noise when T_c is above (below) the design value, and (2) it increases (decreases) the detector saturation power when the T_c is above (below) the design value. At the high (low) edge of the distribution with $T_c = 0.59$ K (0.34 K), there was an 16% (14%) increase (decrease) in the calculated Johnson noise relative to the nominal expected value of $4.0 \text{ pA}/\sqrt{\text{Hz}}$ and a 80%

(68%) increase (decrease) in the calculated phonon noise relative to the nominal expected value of $13 \text{ aW}/\sqrt{\text{Hz}}$. On the low edge of the distribution, the critical temperature causes the 150 GHz detectors to saturate, leaves the responsivity unchanged for the 250 GHz bolometers, and increases the responsivity by 66% for the 410 GHz bolometers. The responsivity is decreased by 110, 56 and 60% for the 150, 250 and 410 GHz bolometers, respectively, on the high edge of the distribution, increasing the readout and Johnson noise relative to phonon and photon noise.

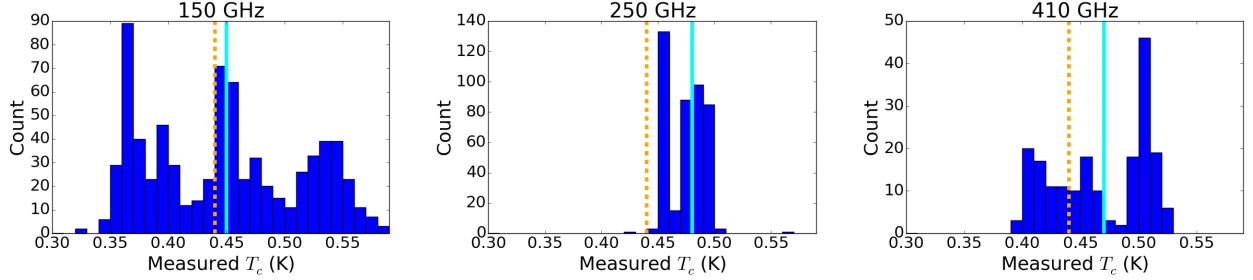


Fig. 13.— Histogram of measured critical temperature values for the detectors in each frequency band including the median (vertical cyan) and design (vertical gold dashed) values.

5.2.3. Average Thermal Conductance

We determine the average thermal conductance of the bolometers using the relation

$$\overline{G}(T_0) = P_{sat}(T_0)/(T_c - T_0), \quad (3)$$

P_{sat} is the power necessary to operate the TES in the regime of strong electrothermal feedback in which the total power absorbed is constant. This power is commonly called the ‘saturation power’ and it depends on the temperature of the bath

$$P_{sat}(T_0) = P_e(T_0) + P_{abs}. \quad (4)$$

Here P_e is the electrical power absorbed in Joule heating and P_{abs} is the radiative power absorbed. In dark conditions we assume that $P_{abs} = 0$, and so $P_{sat}(T_0) = P_{e,d}(T_0)$ is therefore a measurable quantity; we added the subscript $_d$ to $P_{e,d}$ to highlight that this is the electrical power measured in dark conditions.

Histograms summarizing the measured average thermal conductance values for the three EBEX frequency bands are shown in Figure 14. The values of \overline{G} are given for the EBEX bath temperature $T_0 = 0.25 \text{ K}$. The measurements were conducted in three different cryostats, each operating at a different bath temperature $T_{0'}$. We corrected the measured values $\overline{G}(T_{0'})$ to $\overline{G}(T_0)$ using the scaling

$$P_{sat}(T_0) = \left(\frac{T_0^{n+1} - T_0^{n+1}}{T_0^{n+1} - T_{0'}^{n+1}} \right) P_{sat}(T_{0'}), \quad (5)$$

which assumes that the thermal conductivity follows a power law $\kappa = \kappa_0 T^n$; see Section 5.1.3. The design and median of measured values for the average thermal conductances are given in Table 2.

There is appreciable spread in the measured values. This spread is a consequence of variance between wafers and is also apparent in the measurements of T_c . Higher thermal conductance increases phonon noise. For example, for a median 250 GHz detector, phonon noise increased by 10% relative to the nominal value of $20 \text{ aW}/\sqrt{\text{Hz}}$. Higher thermal conductance also increases the required electrical power, decreasing responsivity, which scales as $1/V_{bias}$. With a lower responsivity, noise sources that produce fixed current such as readout noise, are referred to higher noise equivalent power values. In this manner, higher thermal conductance effectively amplifies readout noise.

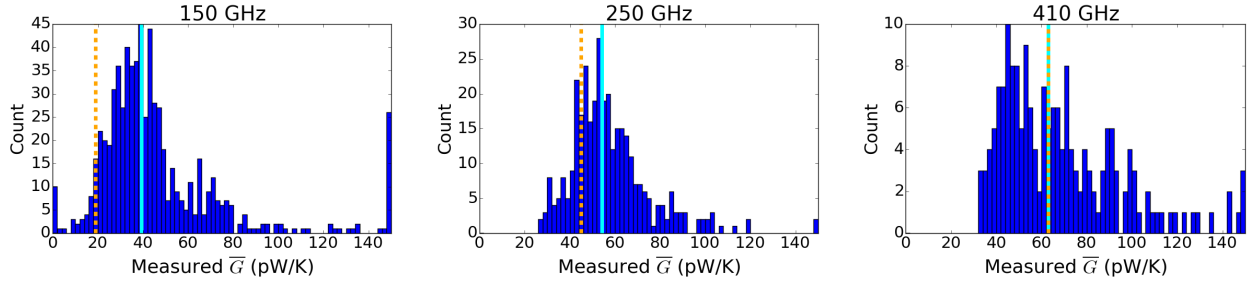


Fig. 14.— Histograms of the measured average thermal conductance values for the three frequency bands including the median (vertical cyan) and design (vertical gold dashed) values. We piled measurements of \bar{G} exceeding 150 pW/K into the last histogram bin.

5.2.4. Detector Time Constants

The effective time constant of the bolometer is given by

$$\tau_{eff} = \frac{\tau_0}{1 + \mathcal{L}}, \quad (6)$$

where \mathcal{L} is the loopgain of the bolometer (Lee et al. 1998).

During the course of the EBEX project we measured time constants in various configurations including a flashing light emitting diode (LED) as part of ‘dark’ measurements, chopping between two optical loads (Hubmayr 2009; Polsgrove 2009), using the phase and amplitude methods during polarization calibration, as described in EP1 and in Klein (2014), and assessing the shapes of cosmic-ray events during flight. Here we report the results from measurements conducted post-flight on three wafers. In contrast with previous measurements, the post-flight ones were all done in identical conditions, using the same method, and have good detector statistics. Each of the three wafers had detectors fabricated for a different frequency band. For the 150, 250, and 410 GHz band wafers there were 88, 97, and 88 active bolometers, respectively.

We used a dedicated cryostat to operate one wafer at a time in dark conditions and at a bath temperature of 0.32 K. We measured τ_{eff} at various operating points along the superconducting transition as quantified by fractions of bolometer normal resistance R_n . We used LEDs with a center wavelength of 940 nm and intrinsic time constant of $1 \mu\text{s}$ to excite the bolometers. The LED was flashed on/off at 13–16 frequencies from 0.1 to 80 Hz for 2 min at each frequency. We calculated

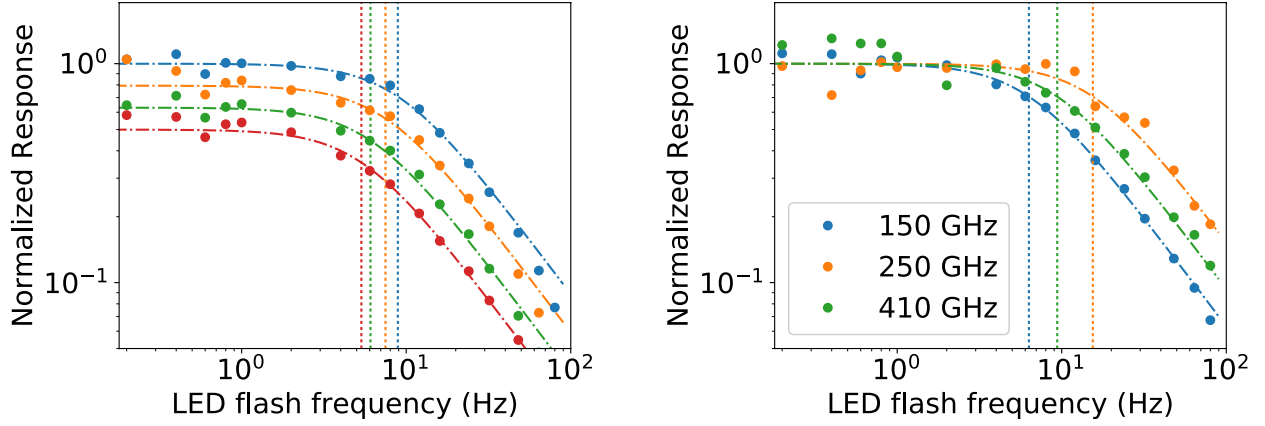


Fig. 15.— Examples of the measured, normalized temporal response of bolometers as a function of LED flash frequency (points), the single pole response fits (dot-dashed), and the 3 dB point (vertical dots). Left: the response of four 150 GHz bolometers biased at $0.8 R_n$. The normalized response is offset vertically for clarity. Right: the response of one bolometer per frequency. All three were tuned to $0.8 R_n$.

the power spectral density of the time stream, removed the background, fit a Fejer kernel (Weiß et al. 2006) to the peak centered on the flash frequency, and extracted the power under the peak from the fit. We plot the response as a function of flash frequency, fit to a single pole function

$$R(f) = \frac{A}{\sqrt{1 + (f/f_c)^2}}, \quad (7)$$

where A is an arbitrary amplitude at $f = 0$, extract the 3 dB cut-off frequency f_c , and convert it to the bolometer time constant

$$\tau_{eff} = \frac{1}{2\pi f_c}. \quad (8)$$

Figure 15 shows a selection of these measurements that are normalized to unity through division by their normalization values A . For each measurement we extracted the error δf_c from the fit’s covariance matrix and propagated it to calculate $\delta \tau_{eff}$. We kept those measurements of τ_{eff} for which $\delta \tau_{eff}/\tau_{eff} < 0.5$ and $\delta \tau_{eff} < 10$ ms. For each wafer the cuts removed between 20% and 50% of the measurements at each point in the transition.

The measured distributions of τ_{eff} for the 150 GHz bolometers are shown in Figure 16. For each wafer and transition depth we found the median of the distribution and plot the medians as a function of transition depth. On all three wafers the width of the distribution was dominated by variations between detectors rather than measurement errors; typical $\delta \tau_{eff}$ values were 1 ms. For all three wafers τ_{eff} qualitatively followed the expectation of $1/(1 + \mathcal{L})$, since \mathcal{L} increases deeper in the transition; see Figure 16.

We measured τ_0 by assuming $\mathcal{L} \ll 1$ at the highest bias point, $0.98 R_n$, so $\tau_{eff} \approx \tau_0$; median τ_0 values are given in Table 2. They are longer than design values by factors of 4–6. We combined the measurements of τ_0 with independent measurement of G to infer bolometer heat capacities. For

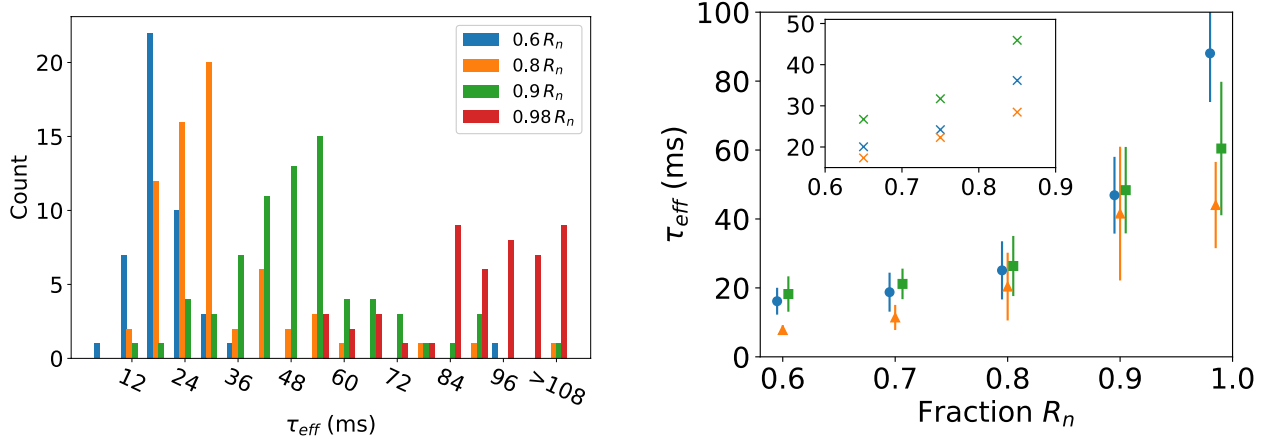


Fig. 16.— Left: distributions of measured τ_{eff} for the 150 GHz wafer at four depths in transition. Right: the median τ_{eff} as a function of the fraction of R_n for the different frequency bands: 150 GHz (blue circles), 250 GHz (orange triangles), and 410 GHz wafer (green squares). Error bars are the standard deviation of the τ_{eff} distributions at each transition depth. We extrapolated laboratory measurements to flight conditions to estimate median time constants at the three transition depths used in flight (inset).

each bolometer we calculated G according to Equation 2 using measured \bar{G} , T_c , n , and a 0.32 K bath temperature. We calculated C for each bolometer and give the design and median of measured values in Table 2. We find that the median heat capacities are larger than design values by factors of 4–8. There are two possible sources for a larger than expected heat capacities: larger specific heats or larger volumes. We measured the thicknesses of the various layers deposited to make the bolometers and find that the volumes were within 15% of design values.

We provided an approximate value for the time constants in flight by extrapolating the thermal conductance to the in-flight 0.25 K bath temperature, and by accounting for changes in \mathcal{L} due to the lower electrical bias of the detectors, which was a consequence of higher in-flight optical load. We did not attempt to correct \mathcal{L} for differences in $\alpha = d(\log R)/d(\log T)$ because the derivatives $\frac{dR}{dT}$ were noisy. The calculated τ_{eff} for the three bias points used in flight are shown in Figure 16. During the majority of flight bolometers were tuned to $0.85 R_n$.

5.3. Radiative Load

Equation 4 quantifies the balance of power between a bolometer and its thermal bath when the total power absorbed P_{abs} is constant. P_{sat} , which depends on the thermal conductance, the transition temperature, and bath temperature, has a characteristic value for each detector and was measured for the majority of the detectors in dark conditions. Although these measurements were done at different bath temperatures T_0 , they were corrected to the operating temperature in flight

T_0 using Equation 5. We use Equation 4 to infer the radiative power absorbed in flight

$$P_{abs,f} = P_{sat}(T_0) - P_{e,f}(T_0) = P_{e,d}(T_0) - P_{e,f}(T_0) \quad (9)$$

where the subscripts d and f denote dark and in-flight conditions, respectively. Figure 17 shows an example of a 150 GHz detector for which $P_{abs,f} = 4$ pW. The electrical power dissipated is plotted as a function of the voltage across the bolometer in dark and flight conditions; these are commonly called ‘load curves’. The difference of 4 pW is measured at the lowest power points of the two load curves, the points at which the bolometer had just entered the constant power operating regime. To ensure stability we operated the detectors as they just entered this regime, that is, relatively high in the superconducting transition. For the majority of the flight the detectors were operated at 85% of their normal resistance.

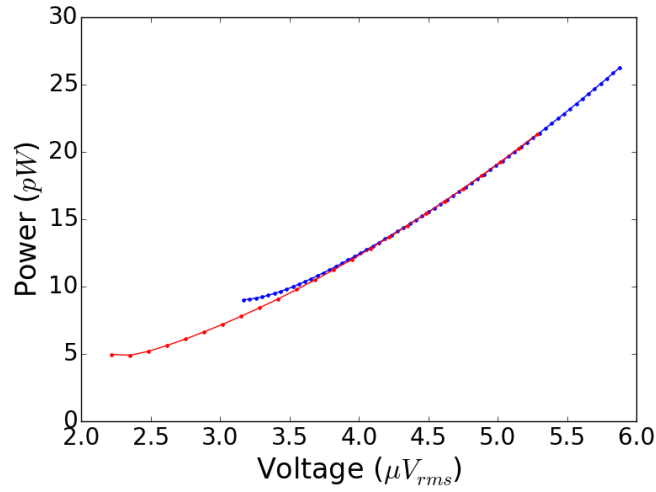


Fig. 17.— Measurements of load curves of a 250 GHz detector in dark conditions (blue) and during flight (red). The detector is operated with voltage bias such that the total power is constant, which is approximately 9 pW in dark conditions. Only 5 pW of electrical power are necessary in flight because absorbed radiative power makes up the difference.

Figure 18 shows the distribution of the radiative load measured by all detectors. We used the load curves measured during the first tuning at float altitude. The elevation (zenith) angle of the telescope was 60° (30°). We measure an average load of 3.6, 5.3, and 5.0 pW for the 150, 250, and 410 GHz detectors, respectively.

5.4. Optical Efficiency

The end-to-end instrument efficiency for a given detector, defined as the ratio of radiative power absorbed by the detector P_{abs} to the radiative power incident on the instrument $P_{inc, inst}$, is the product of the telescope’s transmission ϵ_t and the bolometer absorption efficiency ϵ_b

$$\epsilon = \frac{P_{abs}}{P_{inc, inst}} = \epsilon_t \frac{P_{abs}}{P_{inc}} = \epsilon_t \epsilon_b. \quad (10)$$

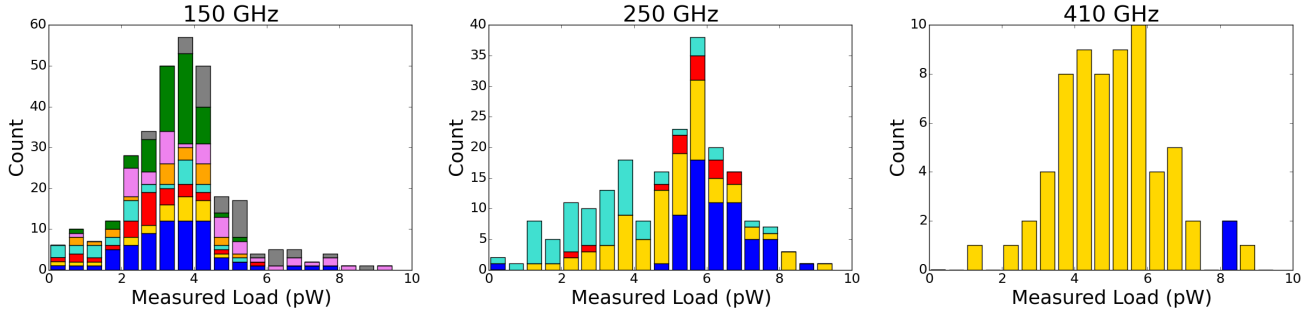


Fig. 18.— Histograms of the measured radiative load from the first detector tuning at float. The different colors represent different wafers. The medians and standard deviations of the distributions are 3.6 ± 1.5 , 5.3 ± 1.8 , and 5.0 ± 1.4 pW, for the 150, 250, and 410 GHz, respectively.

Here P_{inc} is the radiative power incident on a bolometer.

The transmission of the telescope is the product of the transmissions of each of the optical elements. These transmission coefficients were measured or calculated from first principles (Aubin 2012; Zilic 2014) and are summarized in Tables 4 and 5 for the flight and ground measurement configurations, respectively. For absorption we used the optical path length of a representative detector in a given frequency band and extrapolated cryogenic loss tangent values to our temperatures (Jacob et al. 2002).

The calculation of efficiencies required knowledge of the response of the instrument as a function of frequency. These measurements were reported in EP1. The bolometer efficiencies we report here are average efficiencies

$$\langle \epsilon_b \rangle = \frac{1}{\Delta\nu} \int_{\nu_1}^{\nu_2} \epsilon_b(\nu) d\nu, \quad \Delta\nu = \nu_2 - \nu_1, \quad (11)$$

where ν_1 and ν_2 define the bandwidth of the instrument $\Delta\nu$. An absorption efficiency per band is given Table 6 and the results are discussed in Section 5.4.4.

In this section we give constraints on $\langle \epsilon_b \rangle$ using three types of measurements: (a) Galactic plane scans; (b) laboratory cold load, and (c) comparison of laboratory and in-flight optical loads. Only the laboratory cold load measurement is purely laboratory-based.

5.4.1. Galactic Plane Scans

We used passes across the Galactic plane to calibrate the end-to-end response for each detector (Aubin et al. 2016). We assumed the Galactic signal is a sum of *Planck* component maps, which have been scaled to and integrated over each of the bands. We determined the calibration factor $C = dP_{inc,inst}/dI^c$ (in units of W/count) that gave the conversion from power incident on the instrument to current flowing through a bolometer in readout system counts. We related the current in each bolometer in counts to the power absorbed using the current responsivity S_I (A/W) and the conversion from current measured in readout system counts to physical units dI_b^A/dI_b^c (A/count),

Element	150 GHz	250 GHz	410 GHz
Primary mirror	1.00	1.00	1.00
Secondary mirror	1.00	1.00	1.00
Cryostat window	0.97	0.96	0.97
Thermal filter type 4	0.95	0.95	0.95
Thermal filter type 4	0.95	0.95	0.95
Thermal filter type 3	0.98	0.98	0.98
Teflon filter	0.96	0.95	0.93
Thermal filter type 3	0.98	0.98	0.98
LPE1 filter	0.98	0.94	0.98
Thermal filter type 4	0.95	0.95	0.95
LPE2 filter	0.96	0.96	0.98
Field lens	0.97	0.97	0.95
LPE2b filter	0.97	0.99	0.91
HWP	0.94	0.93	0.91
LPE2b filter	0.97	0.99	0.91
Pupil lens #1	0.97	0.96	0.97
Pupil lens #2	0.97	0.96	0.96
Polarizing grid	0.50	0.50	0.50
Camera lens	0.97	0.96	0.97
Low-pass-blocker	0.96	1.00	0.96
Low-pass-edge	0.86	0.95	0.96
Feedhorns	1.00	1.00	1.00
Waveguides	1.00	1.00	1.00
Total	0.23	0.24	0.21

Table 4: Optical elements used during flight and their transmission for each of the frequency bands. These transmissions are used to determine ϵ_t in-flight.

Element	150 GHz	250 GHz	410 GHz
Thermal filter type 1	1.00	0.97	0.93
Thermal filter type 2	0.97	0.96	0.90
Teflon filter	0.96	0.95	0.93
Thermal filter type 3	0.98	0.98	0.98
LPE1 filter	0.98	0.94	0.98
Thermal filter type 4	0.95	0.95	0.95
LPE2 filter	0.96	0.96	0.98
Field lens	0.96	0.97	0.95
LPE2b filter	0.97	0.99	0.91
HWP [†]	0.54	0.53	0.51
Pupil lens #1	0.97	0.95	0.96
Pupil lens #2	0.97	0.95	0.96
Grid	0.50	0.50	0.50
Camera lens	0.97	0.96	0.97
Low-pass-blocker	0.96	1.00	0.96
Low-pass-edge	0.86	0.95	0.96
Feedhorns	1.00	1.00	1.00
Waveguides	1.00	1.00	1.00
Total	0.16	0.15	0.12

[†] At the time of this test the HWP had no antireflection coating.

Table 5: Optical elements used during the ground measurement of absorption efficiency and their transmission for each of the frequency bands.

which was measured in the lab and assumed to be the same for all detectors

$$dP_{abs} = dI^c \frac{dI_b^A}{dI_b^c} \frac{1}{S_I}. \quad (12)$$

Using Equations 10 and 12, the calibration factor is now

$$C = \frac{dP_{inc,inst}}{dI^c} = \frac{1}{\epsilon} \frac{dI_b^A}{dI_b^c} \frac{1}{S_I} = \frac{1}{\epsilon_t \epsilon_b} \frac{dI_b^A}{dI_b^c} \frac{1}{S_I}, \quad (13)$$

from which we find

$$\epsilon_b = \frac{1}{C} \frac{1}{\epsilon_t} \frac{dI_b^A}{dI_b^c} \frac{1}{S_I}. \quad (14)$$

For the responsivity we assumed the slow signal limit and that the detector had large loop gain such that

$$S_I \simeq \frac{\sqrt{2}}{V_b} \quad (15)$$

where V_b was the bolometer’s known voltage bias corrected for the effects of stray impedance (Lee et al. 1998). Figure 19 shows the distributions of inferred average bolometer absorption efficiencies using the calibration factors for all sections of flight and for all detectors. (The calibration factors varied between different sections.) In Table 6 we report the median of each distribution as the absorption efficiency for the respective band. Additional discussion is given in Section 5.4.4.

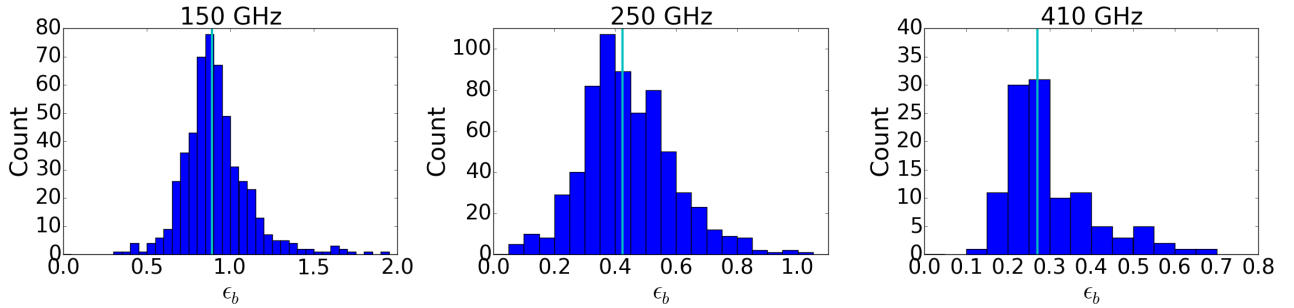


Fig. 19.— Average bolometer absorption efficiency distributions inferred from the calibration factors measured for all valid detectors and sections of the flight. The median efficiencies (vertical cyan) are given in Table 6.

Method	150 GHz	250 GHz	410 GHz
Scans of galactic plane	0.9	0.4	0.3
Cold load	1.0	0.3	0.2

Table 6: Summary of bolometer absorption efficiencies per band extracted using two different methods.

5.4.2. Laboratory Cold Load

We coupled the receiver to a throughput filling, temperature-adjustable cold load. The cold load was constructed to have an emissivity close to 1 in our frequency bands. We set the temperature of the cold load T_{cl} to several values between 25 and 50 K and at each temperature measured the electrical power necessary to operate the bolometer in transition. Similar to Equation 9, the radiative power absorbed by the bolometer in this configuration is given by

$$P_{abs,cl}(T_{cl}) = P_{e,d} - P_{e,cl}(T_{cl}) = \epsilon_b \epsilon_t P_{inc,cl}(T_{cl}), \quad (16)$$

where the subscript $_{cl}$ denotes ‘cold load’. Note that in contrast to Equations 4 and 9 the parametrization of power in Equation 16 is in terms of the load temperature. Following the left side of the equation, we measured the absorbed radiative $P_{abs,cl}$ of each bolometer by differencing the measured saturation power (from the measurement in dark conditions) and the measured electrical power in each of the cold load temperatures. This radiative load is linearly proportional to the radiative load incident on the instrument $P_{inc,cl}$, which we calculated using the spectrum of a black-body load of known temperature, the instruments’ frequency bands, and the transmission efficiencies given in Table 5. The cold load measurement was done for one wafer in each frequency band.

Figure 20 shows an example of $P_{abs,cl}$ as a function of the cold load temperature for one 150 GHz detector, as well as a best-fit model from which we extract its ϵ_b . The Figure also shows the distribution of derived bolometer absorption efficiencies for each frequency band. The medians of the distributions are reported in Table 6. Additional discussion is given in Section 5.4.4.

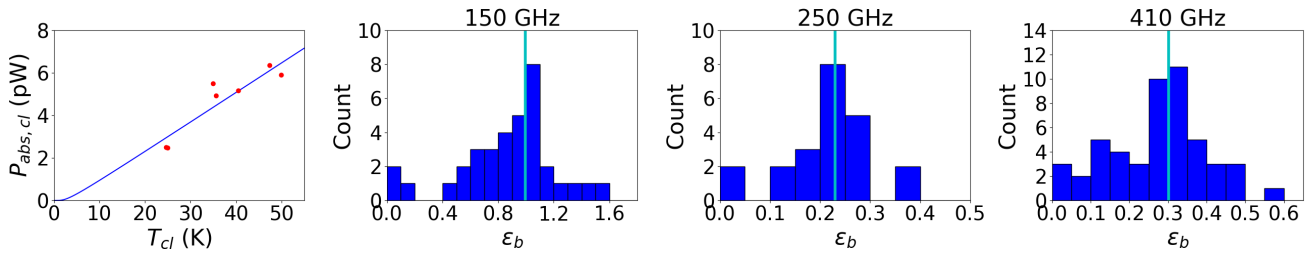


Fig. 20.— Left: measured (red circles) and fitted (solid blue) power absorbed by a 150 GHz bolometer as a function of the cold load temperature. Right: The distribution of measured bolometer absorption efficiency and their median (vertical cyan) for each of the frequency bands. The median values are given in Table 6.

5.4.3. Comparison of Laboratory and in-Flight Optical Loads

A combination of Equations 9 and 10 gives

$$P_{abs,f} = \epsilon_t \epsilon_b P_{inc,inst,f} = P_{e,d}(T_0) - P_{e,f}(T_0), \quad (17)$$

where $P_{inc,inst,f}$ is the radiative power incident on the instrument in flight. We find

$$\epsilon_b = \frac{P_{e,d}(T_0) - P_{e,f}(T_0)}{\epsilon_t P_{inc,inst,f}} = \frac{P_{e,d}(T_0) - P_{e,f}(T_0)}{P_{inc,f}}, \quad (18)$$

where $P_{inc,f}$ is the radiative power incident on the bolometer in flight.

We calculated the power incident on the detectors by including contributions from the sky (CMB and atmospheric emission (Bao 2015)), the mirrors, other optical elements along the optical path, such as the vacuum window and absorptive filters, and the transmission coefficients listed in Table 4 (Aubin 2012); see Table 7. The electrical powers in Equation 18 were known from laboratory and in-flight load curve measurements (see Section 5.3). We found median bolometer absorption efficiencies of 3.4, 1.1, and 0.7 for the 150, 250, and 410 GHz bands, respectively. Bolometer absorption efficiencies larger than 1 are unphysical and we discuss this result in the next Section.

Element	150 GHz (pW)	250 GHz (pW)	410 GHz (pW)
CMB	0.063	0.032	0.0047
Atmosphere	0.0054	0.064	0.37
Mirrors	0.19	0.45	0.76
Instrument	0.36	1.3	3.5
Total	0.62	1.8	4.7

Table 7: Predicted optical power incident on the bolometer during flight $P_{inc,f}$. For each element the power incident on the instrument is higher and is reduced by reflection and absorption by optical elements along the light path. Emission by the instrument is dominated by a 1/2 inch thick teflon filter that had a temperature of 110 K and by the HWP that reached ~ 50 K.

5.4.4. Discussion of Absorption Efficiency Results

The calibration and cold load measurements give approximately consistent results; a relatively high absorption efficiency at the 150 GHz band and medium absorption at the 250 and 410 GHz bands. The calibration measurement is based on the response to changes in the signal level as the instrument passes across the Galactic plane. The scatter in the histograms of Figure 19, which gives some values that are larger than 1, is due primarily to larger uncertainty in the galactic calibration for some of the detectors. The other two measurements are sensitive to the total power absorbed in the detector. The cold load measurement also has some scatter due to noise or systematic errors in the calculation of the absorbed power. For example, it is sometimes challenging to accurately estimate P_e from the load curves such as shown in Figure 17.

The results giving absorption efficiencies larger than 1 for the load curve-based measurement indicate that the denominator in Equation 18 had been underestimated and that there was excess load that was not accounted for by the sources listed in Table 7. Assuming the absorption efficiencies coming from the calibration, we infer excess absorbed load of 3.0, 4.5, and 3.7 pW for the 150, 250, and 410 bands, respectively. These excess loads were not observed with the laboratory cold load. We find total absorbed loads of 3.6, 5.3, and 5.0 pW for the 150, 250, and 410 GHz bands, respectively. We note that the design values for the thermal conductances were based on power saturation values

of 4, 9, and 12 pW, respectively; see Section 5.1.2. Relative to our pre-instrument construction estimates, we find a reduction in sky signal and increase in instrumentally induced load that give a total load consistent with our margin of safety. The reduction in sky signal was a result of having bands with transmission that was approximately half that expected relative to top-hat bands with the same edges.

We hypothesize that beam spill-over past the vacuum window and onto warm surfaces outside of the receiver - here we view the beam as emanating from the focal plane toward the sky - gave rise to the excess load. This spill-over was not detected with the cold load because the load was mounted onto the vacuum window flange and therefore intercepted the entire throughput.

5.5. Noise Performance

We used flight data to quantify individual detectors and overall instrument noise and compare it to expectations. The noise equivalent power (NEP) N , which for brevity we also refer to as ‘noise’, consists of several terms

$$\begin{aligned} N \text{ (W}/\sqrt{\text{Hz}}) &= [N_{\text{photon}}^2 + N_{\text{phonon}}^2 + N_{\text{Johnson}}^2 + N_{\text{readout}}^2]^{1/2} \\ &= \left[\left(2h\nu P_{\text{abs}} + \xi \frac{P_{\text{abs}}^2}{\Delta\nu} \right) + \gamma 4k_B T^2 G + \frac{1}{S_I^2} \cdot \frac{4k_B T}{R} + \frac{1}{S_I^2} \cdot N_{\text{readout}}^2 \right]^{1/2} \end{aligned} \quad (19)$$

where h is Planck’s constant, ν is the center of the observation frequency band, ξ is a unitless number between zero and one quantifying the photon correlation, γ is a unitless number between zero and one accounting for the temperature gradient along the link from the TES to the bath, k_B is Boltzmann’s constant, T is the TES temperature, and R is the TES resistance (Mather 1982).

Time ordered data from flight is used to directly assess N , that is, the left side of Equation 19. We used several configurations to assess the contributions of specific terms on the right side of Equation 19. For each configuration we compared the measurement to expectations. We then combined the contributions in quadrature and compared to the total measured noise N . We determined the combination of N_{Johnson} and N_{readout} using measurements when the detectors were biased above their superconducting transition, N_{phonon} using the measured thermal conductances and critical temperatures, and N_{photon} using the measured radiative load.

To assess any noise contribution X using flight data, we divided the data into segments of 172 s length and made use of all possible segments. Momentary glitches such as cosmic ray hits were replaced with white noise realizations. Sections of data that had more than 10% of their samples flagged as glitches were excluded from the analysis. For each section we removed an offset and a gradient, applied a Hann window, and calculated the spectral density. For the assessment of the readout and Johnson noise, the data was converted from raw digital units (counts) to current referred to the SQUID input (A) using Equation 1. For the assessment of the total NEP, these data were converted from current through the SQUID to power absorbed at the detector by applying the current responsivity S_I

$$X \text{ [W}/\sqrt{\text{Hz}}] = \frac{X \text{ [counts}/\sqrt{\text{Hz}}] \cdot dI_b^A/dI_b^c \text{ [A/count]}}{S_I \text{ [A/W]}}. \quad (20)$$

For each section of data we find the mean level of the spectral density between 3.9 and 4.4 Hz, which is one of the polarization frequency sidebands.

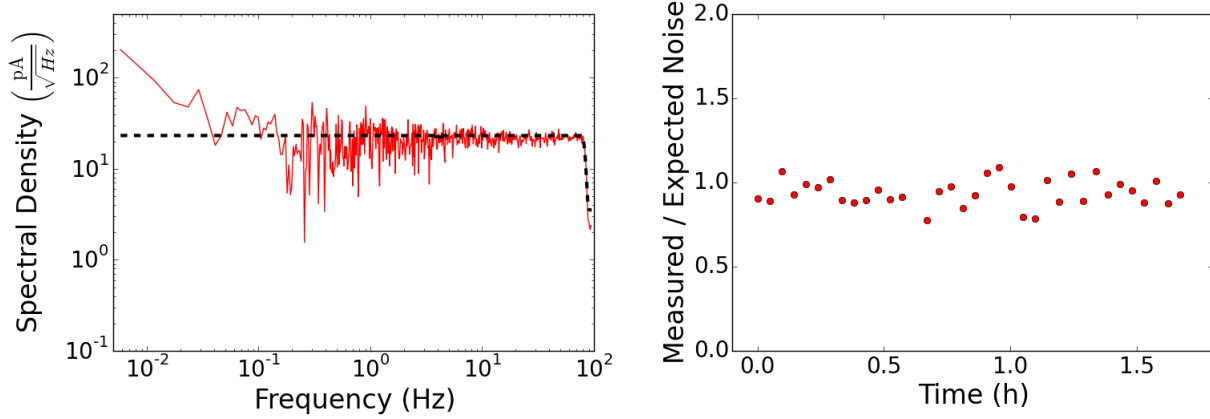


Fig. 21.— Left: the current spectral density of one 150 GHz detector during one 172 s section of the flight when it was overbiased (solid red) and the expected quadrature sum of the Johnson and readout noise (dashed black). We quote noise levels averaged over a narrow band from 3.9 to 4.4 Hz (thick solid black). Right: the measured to expected readout and Johnson noise ratio as a function of time for the same detector.

5.5.1. Johnson and Readout Noise

When the detectors were biased above their superconducting transition - we will use the shorthand ‘overbiased’ - the current responsivity was low and the last two terms in Equation 19 should dominate the overall noise. The spectral density for one section of such data for one detector is shown in the left panel of Figure 21. The measurement is shown in units of $\text{A}/\sqrt{\text{Hz}}$ following Equation 1 since both N_{readout} and N_{Johnson} are intrinsically current noise sources. To assess noise level over time we calculated such spectral density for all valid sections over 1.7 hours of data, about 35 sections per detector. We find that within $\sim 20\%$ the noise levels recorded are stable; see the right panel of Figure 21. Higher variations are expected as compared to the resistor case in Section 4.3 since overbiased detectors have residual sensitivity to stage temperature variations and incident power.

For each detector we calculated the predicted readout noise using the electronic specifications of each element of the readout chain (Aubin 2012). To estimate the Johnson noise we assumed a detector resistance R_n as inferred from the network analysis, and a detector temperature $T = T_c + \Delta P/\bar{G}$, where ΔP is the difference between the electrical power dissipated when the detector is overbiased and P_{sat} measured in dark conditions. We added the predicted contributions from readout and Johnson in quadrature to find a combined noise term (in $\text{A}/\sqrt{\text{Hz}}$). We multiplied this term by a factor 1.7. This is the factor which accounts for the excess noise that was observed with the resistor measurements described in Section 4.3.1. The expected levels shown in Figures 21

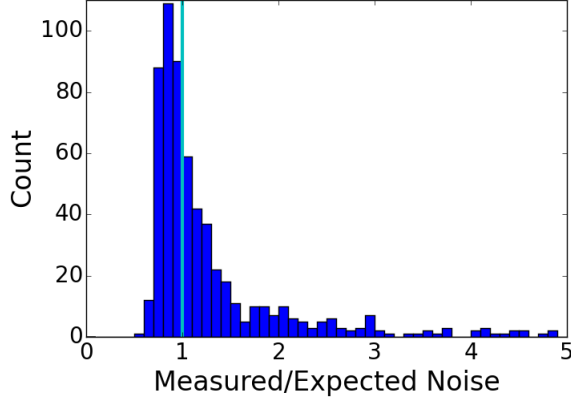


Fig. 22.— Histogram of the median ratio of measured to expected readout and Johnson noise for all bolometers. There are 68 bolometers (not shown) with a ratio greater than 5. The median value (vertical cyan) is 1.0 and the mode is centered at 0.85.

Wafer	Expectation (pA/ $\sqrt{\text{Hz}}$)	Measured/expected ratio
150-09	20	1.1
150-14	18	1.3
150-15	18	0.9
150-39	22	0.8
150-43	24	1.0
150-47	24	1.0
250-23	22	1.0
250-24	26	0.9
250-29	21	1.2
410-28	32	1.0
All detectors		1.0

Table 8: The expected combination of Johnson and readout noise and the ratio of measured to expected levels as measured in-flight for overbiased detectors. For each wafer the ratio is for the median of the distribution for the detectors on that wafer. The first three digits for the wafer number gives its operating frequency band.

and 22 include this extra factor. For each detector and for all sections over the given 1.7 hours of data we formed the ratio of measured to expected noise and found the median. A histogram of the medians for all detectors is shown in Figure 22. Table 8 gives the median ratios for each wafer. The median ratio for all detectors is 1.0.

There was excess noise identified with resistor channels in Section 4.3 amounting to a factor of 1.7 higher than predictions. When this excess is added to predictions of bolometer noise in

the overbias state we find consistency with measurements. We noted in Section 4.3.1 that noise measurements in the overbias state after the North American engineering flight did not exhibit this excess noise. The ratio of measured to predicted noise was 1.0 ± 0.1 (Aubin et al. 2010). These measurements were done in the flight receiver, but the receiver was in the laboratory, without other electromagnetic interference (EMI) sources such as attitude control motors and telemetry transmitters. We therefore hypothesize that EMI contributed additional noise that is most apparent in configurations in which the Johnson and readout noise terms dominate.

5.5.2. Noise Equivalent Power in Transition

The total noise N when the detector operates in its superconducting transition is given by Equation 19. We report on measured N using flight data after removal of the HWPSS (see Section 3). We used all the data that passed quality cuts to be used for astrophysical analysis but also included additional data that would otherwise not be used because of, for example, large pointing errors or scan speeds that were too low.

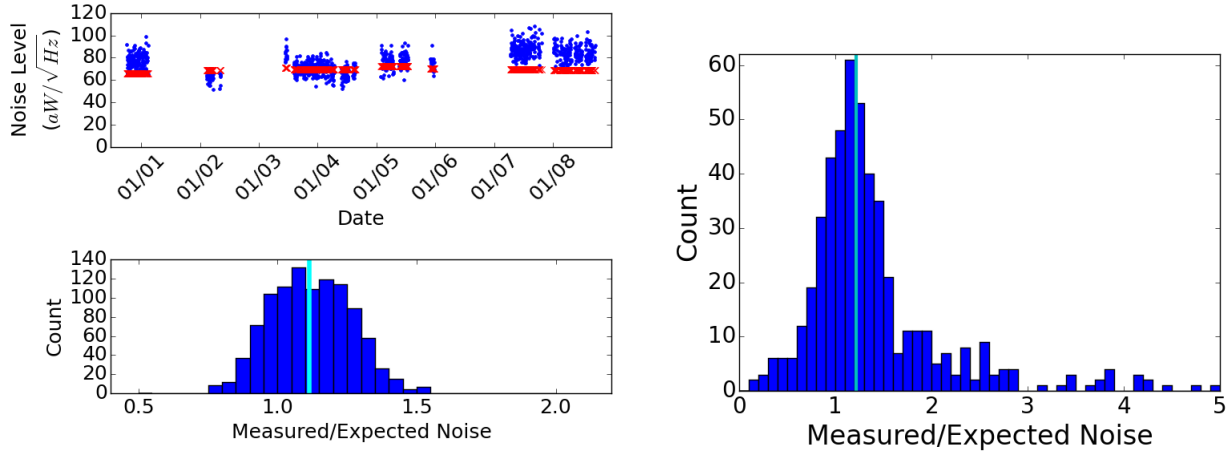


Fig. 23.— Left top: in-transition measured (blue dots) and expected (red crosses) NEP for one 150 GHz detector throughout flight. Gaps indicate times that data is absent or rejected. Left bottom: distribution of measured-to-expected ratio for this detector throughout flight, and the median (vertical cyan) ratio of 1.1. Right: the distribution of the median ratio of measured to expected in-transition noise throughout flight for all bolometers. The median ratio (vertical cyan) is 1.2.

The NEP as a function of time throughout flight for one 150 GHz detector is shown in Figure 23 along with the expected value. We describe the calculation of the expected value in the next paragraph. As before, we found a representative value for the ratio of measured-to-expected NEP throughout flight for a given detector by finding the median over all sections. We combined the medians for each detector to find a median per wafer, which is reported in Table 9. A median measured NEP per frequency band is given in Table 10. Figure 23 gives a histogram for the medians of measured-to-expected ratio for all detectors.

Wafer	Expected NEP [aW/ $\sqrt{\text{Hz}}$]	Measured/expected ratio
150-09	69	1.1
150-14	48	0.7
150-15	57	1.1
150-39	77	1.1
150-43	56	1.2
150-47	64	1.3
250-23	92	1.1
250-24	78	1.4
250-29	98	1.4
410-28	103	1.6
All detectors		1.2

Table 9: The median expected NEP and measured-to-expected ratio for each wafer and combined for all detectors.

We calculated an expected NEP by finding the theoretical Johnson and readout current noise terms and multiplying them by (1) a factor of 1.7 coming from the excess noise in the resistor measurements (see Section 4.3.1), and (2) by an additional factor per wafer as listed in Table 8. The second factor has been identified through the noise measurement with overbiased detectors (see Section 5.5.1). To convert from current noise to NEP we divided the Johnson and readout noise terms by the current responsivity and assumed the high loopgain limit. We assumed $\gamma = 0.5$ to predict the phonon noise (Mather 1982). We calculated photon noise using the measured radiative load per detector, as described in Section 5.3. We quote the predicted level for a photon correlation factor of 1. The median predictions decreases by 20% (7%) when using a correlation factor of 0 for the 150 and 250 (410) GHz bands.

For the 150 band the measured noise is broadly consistent with calculations after accounting for the excess noise identified through measurements with resistors. No further excess noise is identified when operating the bolometers in transition. The average noise increase for the 3 (1) wafers at 250 (410) GHz is about 30 (60)% after accounting for the excess noise. This level is at the border or beyond the 20-30% uncertainties in our estimates. This additional source of noise is being investigated, although the small number of available wafers may give a biased impression of trends.

6. Noise Equivalent Temperature and Map Depth

We estimated the noise equivalent temperature (NET) in two ways: (1) using the TOD in counts and the calibration factors that convert count to temperature; (2) converting the measured NEP to NET. The term ‘temperature’ refers to equivalent sky CMB temperature fluctuations. In this section we describe the two methods and show that they give consistent results. We then use the measured NET and the instantaneous attitude information to produce depth maps for each of

Noise source	Value ($aW/\sqrt{\text{Hz}}$)		
	150 GHz	250 GHz	410 GHz
Readout	$\sqrt{2} \cdot 15$	$\sqrt{2} \cdot 15$	$\sqrt{2} \cdot 23$
Johnson	$\sqrt{2} \cdot 7.6$	$\sqrt{2} \cdot 8.2$	$\sqrt{2} \cdot 13$
Phonon	22	25	32
Photon	32	49	63
Excess	43	64	133
Total	62	88	160

Table 10: The median NEP contributions to noise measured in-transition for each frequency band.

the frequency bands.

6.1. NET using the TOD and Calibration

For each detector we calculated power spectral densities of 5.7 min sections of calibrated, deglitched, HWPSS-subtracted TOD, and fit them with a three-parameter noise model $M(f)$ consisting of red and white noise terms as a function of frequency

$$M(f) = W^2 \left[1 + \left(\frac{f_k}{f} \right)^\alpha \right]. \quad (21)$$

The parameters are W^2 , the white noise level (in K^2/Hz); f_k , the frequency cutoff of the red noise power law (also referred to as f_{knee} , in Hz); and α , the red noise spectral index. We used all calibrated data throughout flight that passed quality cuts for astrophysical analysis, see Didier (2016), and added other data with valid noise information but that would not pass cuts for making maps. Such data included sections during times at which the attitude reconstruction was poor or the scan speeds were below or above specific thresholds. A polynomial with up to cubic terms in time was subtracted from the TOD before applying a Hann window and calculating the power spectral density (PSD). Figure 24 shows an example of a PSD and its model fit for one section of the data of a 250 GHz detector.

The fitting - conducted on at least 10 sections of data for each detector, but typically over many hours of data - generated a set of parameters W , f_k , and α , with which we characterized the noise performance. For each detector we find the three median parameter values over all flight. We histogram these median values for all available detectors per frequency band in Figures 25, 26, and 27. The Figures also give the medians of the distributions.

The data show knee frequencies near 200 mHz and red noise power law index near 2.3. These relatively high values are not intrinsic to the detectors or readout, but rather are a consequence of the azimuth motor malfunction, described in EP3. In the absence of controlled azimuth pointing the payload executed full rotations causing strong Sun-synchronous drifts in the TOD. Removal of a cubic order polynomial from the TOD removes some of the drifts, but remnants are manifest in

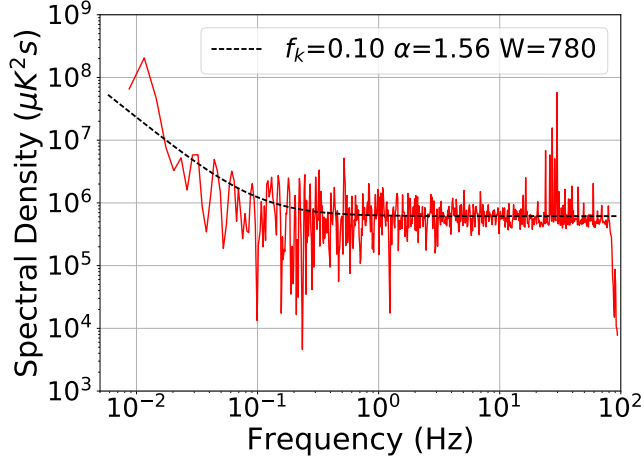


Fig. 24.— Example PSD (solid red) for one section of a 250 GHz bolometer data with fit (dashed black) to the noise model of Equation 21.

the statistics of f_k and α . A correlation analysis between the noise properties of different detectors showed strong coherency at low frequencies supporting the model of drifts due to Sun-synchronous signals.

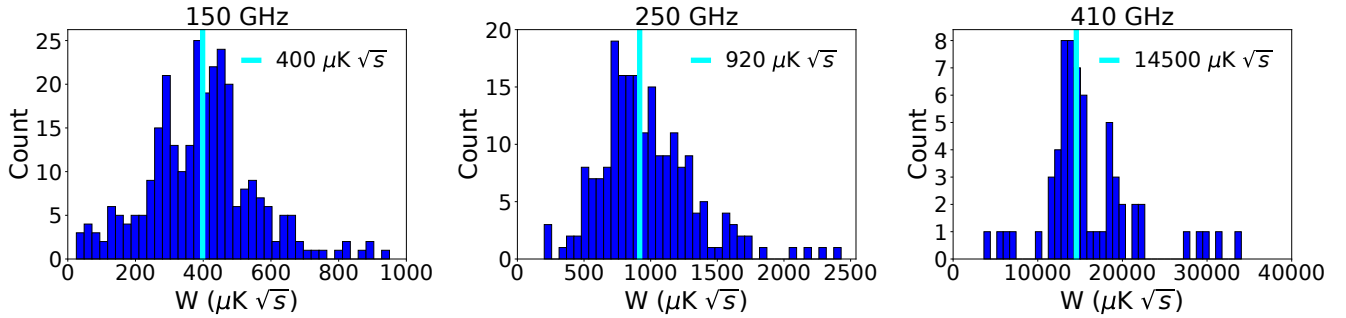


Fig. 25.— Distribution of median NET for all available detectors in a given frequency band and the median of the distribution (vertical cyan).

6.2. NET using the NEP

We converted the measured NEP to NET using

$$\text{NET}(\mu\text{K}\sqrt{\text{s}}) = \text{NEP}(\text{W}/\sqrt{\text{Hz}}) \left(\frac{dT}{dP} \right) \bigg|_{T_{\text{CMB}}} \frac{1}{\sqrt{2}}, \quad (22)$$

where $\left(\frac{dT}{dP} \right) \bigg|_{T_{\text{CMB}}}$ is a conversion factor from absorbed power to temperature calculated using the throughput, measured bands, and efficiency. For NEP we used the median calculated for all de-

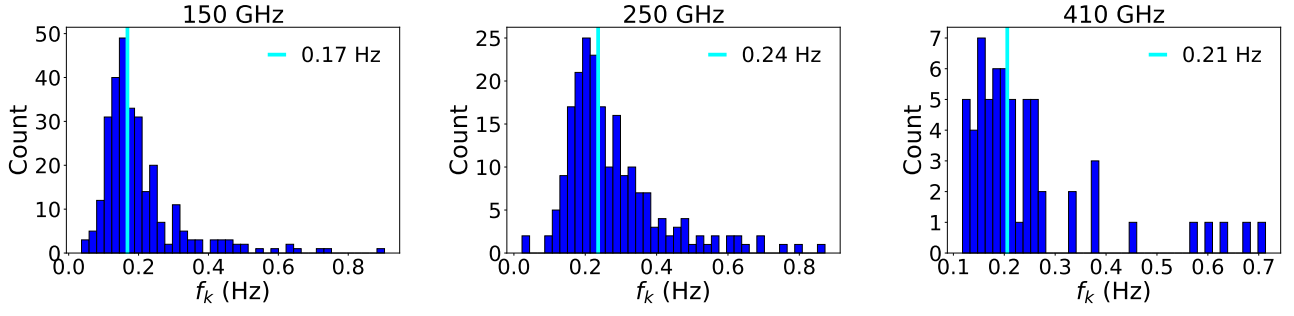


Fig. 26.— Distribution of median knee frequencies for all available detectors in a given frequency band and the median of the distribution (vertical cyan).

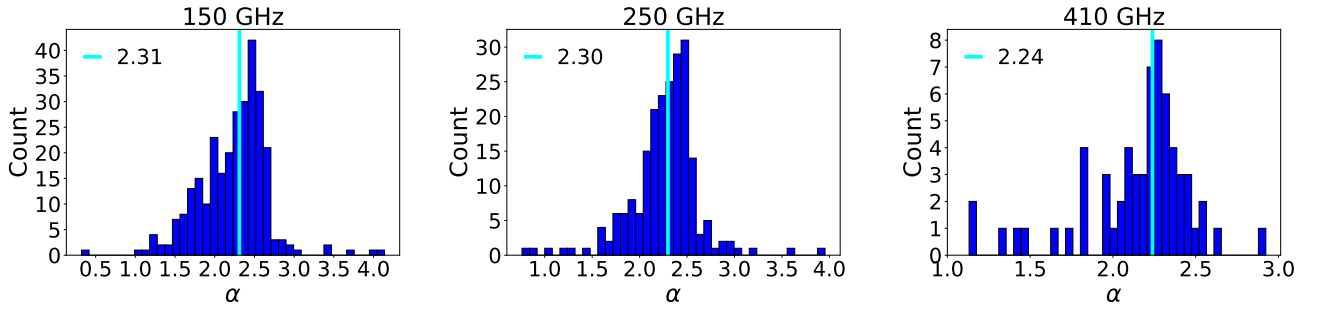


Fig. 27.— Distribution of median red noise power indices for all available detectors in a given frequency band and the median of the distribution (vertical cyan).

tectors in a given frequency, as listed in Table 11. The measured NETs are consistent within 10% for the 150 and 250 GHz bands. There is a larger difference for the 410 GHz. The estimate from the NEP depends on the product of the instrument’s throughput and efficiency through the multiplicative factor dT/dP ; see Equation 22. For the throughput we assumed a single mode for the propagating electromagnetic wave. We hypothesize that at the higher frequency band we are underestimating the throughput by assuming a complete cut-off of the 2nd mode. A 25% higher throughput brings the NET from NEP and NET from calibration to values that agree within our overall uncertainty.

	150 GHz	250 GHz	410 GHz
NEP ($\text{aW}/\sqrt{\text{Hz}}$)	62	88	160
NET from NEP ($\mu\text{K } \sqrt{\text{s}}$)	380	1000	23000
NET from Calibration ($\mu\text{K } \sqrt{\text{s}}$)	400	920	14500

Table 11: The median measured NEP per frequency band and comparison of NET calculated from the NEP using the measured efficiency, frequency bands and assumed throughput, and the NET measured using the calibration.

6.3. Map Depth

The high fidelity attitude reconstruction from the EBEX2013 flight was discussed in EP3. We binned all the data that passed quality cuts for making maps using HEALPix (Górski et al. 2005) with $n_{\text{side}} = 64$. With each sample we associated an equivalent temperature noise N_s (in μK) equal to the product of the NET calculated during that time section and the square root of the sampling rate. We calculated depth per pixel D_p following

$$D_p = \left(\sum \frac{1}{N_{s,p}^2} \right)^{-1/2}, \quad (23)$$

where the sum is over all samples that had pointing associated with a given pixel p .

The depth maps with pixels of $\sim 1 \text{ deg}^2$ for the three frequency bands are shown in Figure 28. The noise distribution is strongly inhomogeneous, a consequence of an azimuth motor malfunction, as described in EP3. The median depth values per pixel for the 150 and 250 GHz bands - 11 and 28 μK , respectively - are several factors larger than those reported by *Planck* and the expected CMB E-mode signal. A signal-to-noise ratio above 1 is only achieved for a fraction of the pixels on the Galaxy at 410 GHz. The depth maps do not encode $1/f$ noise and filtering that further degrades the signal-to-noise ratio. We therefore decided not to publish maps.

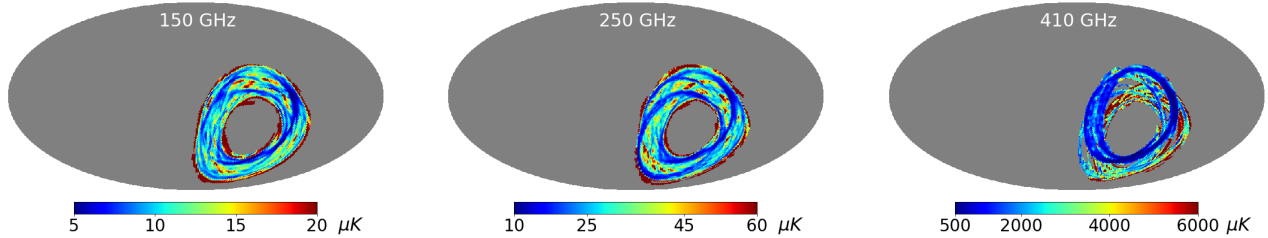


Fig. 28.— Depth maps using the NET and attitude reconstruction from the EBEX2013 flight. The maps use HEALPix $N_{\text{side}} = 64$ pixels and the color scale is linear. At this pixelization the median pixel noise is 11, 28 and 1982 μK for the 150, 250, and 410 GHz bands, respectively.

7. Summary

EBEX was a CMB polarimeter that had two focal plane consisting of 14 detector wafers. Each focal plane had 4 wafers operating at 150 GHz, two at 250 GHz, and a central wafer at 410 GHz. We presented the design of bolometers optimized for the low optical load in the stratosphere and for operation at 410 GHz, a frequency that is unique for balloon payloads. To handle the thin wafers suitable for this frequency band we developed a technique to bond them to thicker wafers. We showed distributions of measured thermal conductances, normal resistances, transition temperatures, and time constants. For the 250 and 410 GHz bands the median thermal conductances

were within 20% of design values. For the 150 GHz band, for which our target was 2.4 times lower than for the 250 GHz band, the median measured value was 2 times higher than design reflecting the additional challenge in making very low thermal conductance spider web bolometers that are operating at 0.25 K. The measured transition temperatures were within 10% of design values and median measured (design) saturation powers were 7.8 (4), 12 (9) and 14 (12) pW, for the 150, 250, and 410 GHz, respectively. The measured time constants were 3.5 to 5.7 times longer than design values. Either published values for specific heats of the materials that made up the bolometer are incorrect, or the devices had been contaminated by unknown materials during fabrication.

We measured in-flight median optical loads of 3.6, 5.3, and 5.0 pW, at the three bands, respectively. Given the final configuration of all optical elements inside the instrument and the measured frequency bands, we calculated the expected contributions from the sky, warm telescope, and instrument emission. The warm mirrors, a teflon filter, and the HWP dominated the expected load. We have also identified excess optical load in flight, but no excess load was measured when we coupled a 4 K load onto the vacuum window of the receiver in the laboratory. We therefore attribute the additional load to spillover of throughput onto warm surfaces outside of the receiver.

Two measurement methods for finding the bolometer absorption efficiencies gave consistent results within 10% for all frequency bands. They indicate high absorption efficiency (~ 0.9) for the 150 GHz and medium (medians of ~ 0.35 and ~ 0.25) for the 250 and 410 GHz bands. The measured distributions are broad occasionally giving apparently unphysical absorption values larger than 1. However, noisy measurements that give wide distributions can give values larger than 1.

EBEX was the first experiment to implement the digital version of a frequency domain multiplexing system aboard a balloon payload. For several years it had the highest multiplexing factor of 16 until SPT3G began implementing a multiplexing factor of 64 in 2016. We developed novel, superconducting, low inductance microstrips. We measured gain stability of better than 0.25% over 13 hours, and better than 2% over the duration of the flight, even as the temperature of the readout boards experienced temperature excursions of up to 20°C.

The rotation of the HWP introduced a HWP synchronous signal in the TOD. To assess the noise performance we fit and removed the synchronous signal. We gave a detailed accounting of the measured noise. The readout noise was measured to match predictions in the laboratory and for dark SQUIDS in flight. We found excess noise in-flight when analyzing resistor data and when the detectors were in an over-biased state, for which the readout and Johnson noise are expected to be dominant. The median excess noise was a factor 1.7 larger than the expected total of Johnson and readout noise terms. When we included an extra noise term to account for the excess noise observed in the over-bias state the median measured noise in-transition was 20% higher than expectation. We suspect that electromagnetic pickup from telemetry electronics coupling to the long microstrips was the cause for the excess noise.

We calculated the median NET in two ways and found consistency for the 150, and 250 GHz bands. The pre-flight expectation for 150 GHz, taking into account the high thermal conductivity detectors, but without excess noise or load, was $210 \mu\text{K}\sqrt{s}$. For the target thermal conductivity of 19 pW/K, the expectation was $180 \mu\text{K}\sqrt{s}$, a factor of 2.2 lower than the achieved value of

400 $\mu\text{K}\sqrt{s}$. Our expectation of 180 $\mu\text{K}\sqrt{s}$ was higher by a factor of 1.3 compared to the best reported by BOOMERANG (Crill et al. 2003) (which also had bolometers operated at a bath temperature near 0.25 K) because EBEX had two warm mirrors, not one, higher internal emission from a teflon filter due to a much larger vacuum window, higher temperature for its rotating HWP, and higher detector thermal conductivity than required at 150 GHz. We chose high detector thermal conductance because it mitigated the risk of un-anticipated optical load at the expense of higher noise. This choice proved prudent; we did experience excess load but continued to operate the majority of the bolometers. A next generation balloon-borne instrument that has only one ambient temperature mirror, detectors with appropriately low thermal conductivity, and that applies the lessons learned from EBEX2013 (including having lower internal emission from filters and HWP, and mitigating excess load and noise) can achieve 140 $\mu\text{K}\sqrt{s}$ at 150 GHz.

EBEX was the first balloon experiment to implement a kilo-pixel array of bolometers in the focal plane. It was among the first to face the challenges imposed by a significantly larger focal plane, optical elements, and vacuum window. The EBEX experience suggests the following path for a future experiment with kilo-pixel TES arrays to make optimal use of the balloon environment: (1) reduce instrument emissions through the development and implementation of high thermal conductance, low mm-wave emissivity and reflectivity IR filters and lenses, and by maintaining optical elements at cold temperatures if practical. However, for an experiment that targets a resolution finer than ~ 25 arcmin at 150 GHz, at least one reflector will almost certainly still need to be maintained at ambient temperatures; (2) implement optical elements that are appreciably larger than the nominal optical bundle to mitigate diffraction near apertures and thus reduce spill-over outside the designated throughput, even at the expense of a larger cryostat, larger window, and potentially heavier payload; (3) pay attention to EMI mitigation, as wiring that couple the SQUIDs to the detector focal plane are susceptible to the transmitter-heavy environment on-board the payload. (Since the EBEX2013 flight there have been additional reports of excess noise due to telemetry electronics in other millimeter and sub-millimeter experiments.) The EMI integrity of the wiring cavity of the cryostat should be excellent or experiments should impose radio-silence after initial check-up and calibration. Significant time should be allocated to testing in full flight configuration, including telemetry electronics.

Because of the malfunction of the azimuth motor, a result of thermal design error that is discussed in EP3, the instrument scanned $\sim 6000 \text{ deg}^2$, giving shallow depth with highly inhomogeneous noise. We presented depth maps that gave a median noise of 11 and 28 μK per HEALPix-Nside = 64 pixel at 150 and 250 GHz. The map noise is higher compared to *Planck*'s noise as well as to that of other contemporaneous experiments and we did not find it compelling to publish our own maps or power spectra.

EBEX pioneered the use of TES bolometers on a balloon-borne platform. It was the first experiment to fly a small array of these detectors in a test-flight in 2009 and a kilo-pixel array during its EBEX2013 flight. Nearly 1000 bolometers were operating shortly after the payload reached float altitude. EBEX pioneered the use of the digital frequency domain multiplexing readout system. This system is now implemented on several operating ground-based instruments and is baselined for a proposed space mission. EBEX was also the first astrophysics experiment to implement a

superconducting magnetic bearing. This system too is baselined for a ground-based and a proposed space mission. EBEX was a successful technology pathfinder for future CMB space missions.

Support for the development and flight of the EBEX instrument was provided by NASA grants NNX12AD50G, NNX13AE49G, NNX08AG40G, and NNG05GE62G, and by NSF grants AST-0705134 and ANT-0944513. We acknowledge support from the Italian INFN INDARK Initiative. Ade and Tucker acknowledge the Science & Technology Facilities Council for its continued support of the underpinning technology for filter and waveplate development. We also acknowledge support by the Canada Space Agency, the Canada Research Chairs Program, the Natural Sciences and Engineering Research Council of Canada, the Canadian Institute for Advanced Research, the Minnesota Supercomputing Institute, the National Energy Research Scientific Computing Center, the Minnesota and Rhode Island Space Grant Consortia, our collaborating institutions, and Sigma Xi the Scientific Research Society. Research described in this paper used facilities of the Midwest Nano Infrastructure Corridor (MINIC), a part of the National Nanotechnology Coordinated Infrastructure (NNCI) program of the National Science Foundation. Baccigalupi acknowledges support from the RADIOFOREGROUNDS grant of the European Union’s Horizon 2020 research and innovation program (COMPET-05-2015, grant agreement number 687312). Didier acknowledges a NASA NESSF fellowship NNX11AL15H. Reichborn-Kjennerud acknowledges an NSF Post-Doctoral Fellowship AST-1102774, and a NASA Graduate Student Research Fellowship. Raach and Zilic acknowledge support by the Minnesota Space Grant Consortium. The Flatiron Institute is supported by the Simons Foundation. Feeney was partially supported by the UK Science and Technology Facilities Council (STFC). We very much thank Danny Ball and his colleagues at the Columbia Scientific Balloon Facility for their dedicated support of the EBEX program. We thank Darcy Baron and Kaori Hattori for inputs on the stray inductance of the microstrips.

REFERENCES

- Ade, P., Akiba, Y., Anthony, A., et al. 2014, *ApJ*, 794, doi:2/171
- Araujo, D. 2017, PhD thesis, Columbia University
- Aubin, F. 2012, PhD thesis, McGill University
- Aubin, F., Aboobaker, A. M., Ade, P., et al. 2010, in *Proc. SPIE*, Vol. 7741, Millimeter, Submillimeter, and Far-Infrared Detectors and Instrumentation for Astronomy V, 77411T–77411T–10
- Aubin, F., Aboobaker, A. M., Ade, P., et al. 2016, ArXiv e-prints, arXiv:1601.07923
- Bao, C. 2015, PhD thesis, University of Minnesota
- Baumann, D., Jackson, M. G., Adshead, P., et al. 2009, *AIPC*, 1141, 10
- BICEP2 Collaboration, Ade, P. A. R., Aikin, R. W., et al. 2014, *Physical Review Letters*, 112, 241101
- BICEP2/Keck and Planck Collaborations, Ade, P. A. R., Aghanim, N., et al. 2015, *Phys. Rev. Lett.*, 114, 101301
- Bock, J. J., Chen, D., Mauskopf, P. D., & Lange, A. E. 1995, *Space Sci. Rev.*, 74, 229
- Chang, C. L., Ade, P. A. R., Aird, K. A., et al. 2009, *AIP Conference Proceedings*, 1185, 475
- Chapman, D. 2015, PhD thesis, Columbia University
- Chapman, D., Didier, J., Hanany, S., et al. 2014, in *Proc. SPIE*, Vol. 9152, Software and Cyberinfrastructure for Astronomy III, 915212
- Chapman, D., Aboobaker, A. M., Araujo, D., et al. 2015, in *2015 IEEE Aerospace Conference*, 1–11
- Crill, B. P., Ade, P. A. R., Artusa, D. R., et al. 2003, *The Astrophysical Journal Supplement Series*, 148, 527
- Didier, J. 2016, PhD thesis, Columbia University
- Didier, J., Chapman, D., Aboobaker, A., et al. 2015, *Proc. of IEEE Aerospace Conference*
- Didier, J., Miller, A. D., Araujo, D., et al. 2017, in prep
- Dobbs, M., Bissonnette, E., & Spieler, H. 2008, *IEEE Transactions on Nuclear Science*, 55, 21
- Dobbs, M. A., Lueker, M., Aird, K. A., et al. 2012, *Review of Scientific Instruments*, 83, 073113
- Glenn, J., Chattopadhy, G., Edgington, S., et al. 2002, *Applied Optics*, 41, 136
- Górski, K. M., Hivon, E., Banday, A. J., et al. 2005, *ApJ*, 622, 759

- Grainger, W., Aboobaker, A. M., Ade, P., et al. 2008, in Proc. SPIE, Vol. 7020, Millimeter and Submillimeter Detectors and Instrumentation for Astronomy IV, 70202N
- Hanson, D., Hoover, S., Crites, A., et al. 2013, PhRvL, 111, 141301
- Huber, M. E., Neil, P. A., Benson, R. G., et al. 2001, IEEE Transactions on Applied Superconductivity, 11, 4048
- Hubmayr, J. 2009, PhD thesis, University of Minnesota
- Hubmayr, J., Aubin, F., Bissonnette, E., et al. 2008, in Proc. SPIE, Vol. 7020, Millimeter and Submillimeter Detectors and Instrumentation for Astronomy IV, 70200J–70200J–8
- Irwin, K. D., & Hilton, G. C. 2005, Transition-Edge Sensors (Springer Berlin Heidelberg), 63
- Jacob, M. V., Mazierska, J., Leong, K., & Krupka, J. 2002, IEEE Transactions on Microwave Theory Techniques, 50, 474
- Johnson, B. R., Collins, J., Abroe, M. E., et al. 2007, ApJ, 665, 42
- Kes, P. H., Rolfes, J. G. A., & de Klerk, D. 1974, Journal of Low Temperature Physics, 17, 341
- Klein, J. 2014, PhD thesis, University of Minnesota
- Klein, J., Aboobaker, A., Ade, P., et al. 2011, in Proc. SPIE, Vol. 8150, Cryogenic Optical Systems and Instruments XIII, 815004–815004–10
- Kovac, J. M., Leitch, E. M., Pryke, C., et al. 2002, Nature, 420, 772
- Lamb, J. W. 1996, International Journal of Infrared and Millimeter Waves, 17, 1997
- Lanting, T. M. 2006, PhD thesis, University of California, Berkeley
- Lee, A. T., Richards, P. L., Nam, S. W., Cabrera, B., & Irwin, K. D. 1996, Applied Physics Letters, 69, 1801
- Lee, S.-F., Gildemeister, J. M., Holmes, W., Lee, A. T., & Richards, P. L. 1998, Applied Optics, 37, 3391
- MacDermid, K. 2014, PhD thesis, McGill University
- MacDermid, K., Hyland, P., Aubin, F., et al. 2009, in American Institute of Physics Conference Series, Vol. 1185, American Institute of Physics Conference Series, ed. B. Young, B. Cabrera, & A. Miller, 253–256
- MacDermid, K., Aboobaker, A. M., Ade, P., et al. 2014, in Proc. SPIE, Vol. 9153, Millimeter, Submillimeter, and Far-Infrared Detectors and Instrumentation for Astronomy VII, 915311
- Mather, J. C. 1982, Appl Opt, 21, 1125

- Milligan, M., Ade, P., Aubin, F., et al. 2010, in Proc. SPIE, Vol. 7740, Software and Cyberinfrastructure for Astronomy, 774007
- Naess, S., Hasselfield, M., McMahon, J., et al. 2014, JCAP, 2014, 007
- NIST. 2010, Private Communication, ,
- Oxley, P., Ade, P. A., Baccigalupi, C., et al. 2004, in Proc. SPIE, Vol. 5543, Infrared Spaceborne Remote Sensing XII, 320–331
- Phillips, T. G., & Zmuidzinas, J., eds. 2003, Proc. SPIE, Vol. 4855, Design and performance of feedhorn-coupled bolometer arrays for SPIRE, ed. T. G. Phillips & J. Zmuidzinas, 510–519
- Polsgrove, D. E. 2009, PhD thesis, University of Minnesota
- Reichborn-Kjennerud, B. 2010, PhD thesis, Columbia University
- Reichborn-Kjennerud, B., Aboobaker, A. M., Ade, P., et al. 2010, in Proc. SPIE, Vol. 7741, Millimeter, Submillimeter, and Far-Infrared Detectors and Instrumentation for Astronomy V, 77411C
- Sagiv, I., Aboobaker, A. M., Bao, C., et al. 2012, in Twelfth Marcel Grossmann Meeting on General Relativity, ed. A. H. Chamseddine, 2166–2176
- Sagiv, I. S. 2011, PhD thesis, University of Minnesota
- Schwan, D., Ade, P. A. R., Basu, K., et al. 2011, Review of Scientific Instruments, 82, doi:<http://dx.doi.org/10.1063/1.3637460>
- Scott, D., & Smoot, G. F. 2010, in The Review of Particle Physics, ed. K. Nakamura *et al.* (J. Phys.)
- Silva-Feaver, M., Arnold, K., Barron, D., et al. 2017
- Suzuki, A. G. 2013, PhD thesis, University of California, Berkeley
- Takakura, S., Aguilar, M., Akiba, Y., et al. 2017, arXiv:1702.07111
- The EBEX Collaboration. 2016a, ApJ
- . 2016b, ApJ
- Van Sciver, S. 2012, Helium Cryogenics (Springer), doi:10.1007/BF00751274
- Weiß, A., Wellein, G., Alvermann, A., & Fehske, H. 2006, Reviews of Modern Physics, 78, 275
- Westbrook, B., Lee, A., Meng, X., et al. 2012, Journal of Low Temperature Physics, 167, 885
- Westbrook, B. G. 2014, PhD thesis, University of California, Berkeley
- Yoon, J., Clarke, J., Gildemeister, J. M., et al. 2001, Applied Physics Letters, 78, 371

Zaldarriaga, M., & Seljak, U. 1997, Phys. Rev. D, 55, 1830

Zilic, K. 2014, PhD thesis, University of Minnesota